Amoxicillin-resistant *Streptococcus pneumoniae* can be resensitized by targeting the mevalonate pathway as identified by sCRilecs-seq

Liselot Dewachter[a], Xue Liu[a,b], Julien Dénéréaz[a], Vincent de Bakker[a], Charlotte Costa[c], Mara Baldry[c], Jean-Claude Sirard[c], Jan-Willem Veening[a]*

[a] Department of Fundamental Microbiology, Faculty of Biology and Medicine, University of Lausanne, Biophore Building, Lausanne 1015, Switzerland

[b] Guangdong Key Laboratory for Genome Stability and Human Disease Prevention, Department of Pharmacology, International Cancer Center, Shenzhen University Health Science Center, 518060 Shenzhen, China

[c] Univ. Lille, CNRS, Inserm, CHU Lille, Institut Pasteur Lille, U1019 - UMR 9017 - CIIL - Center for Infection and Immunity of Lille, F-59000 Lille, France

*Correspondence to: jan-willem.veening@unil.ch Twitter: @JWVeening

Abstract

Antibiotic resistance in the important opportunistic human pathogen *Streptococcus pneumoniae* is on the rise. This is particularly problematic in the case of the β-lactam antibiotic amoxicillin, which is the first intention therapy. It is therefore crucial to uncover targets that would kill or resensitize amoxicillin-resistant pneumococci. To do so, we developed a genome-wide, single-cell based, gene silencing screen using CRISPR interference called sCRilecs-seq (subsets of CRISPR interference libraries extracted by fluorescence activated cell sorting coupled to next generation sequencing). Since amoxicillin affects growth and division, sCRilecs-seq was used to identify targets that are responsible for maintaining proper cell size. Our screen revealed that downregulation of the mevalonate pathway leads to extensive cell elongation. We show that this phenotype is caused by insufficient transport of cell wall precursors across the cell membrane due to a limitation in the production of undecaprenyl phosphate (Und-P), the lipid carrier responsible for this process. The data suggest that septal peptidoglycan synthesis is more sensitive to reduced Und-P levels than peripheral peptidoglycan synthesis. We successfully exploited this knowledge to create a combination treatment strategy where the FDA-approved drug clomiphene, an inhibitor of Und-P synthesis, is paired up with amoxicillin. Our results show that clomiphene potentiates the antimicrobial activity of amoxicillin and that combination therapy resensitizes amoxicillin-resistant *S. pneumoniae*. These findings could provide a starting point to develop a solution for the increasing amount of hard-to-treat amoxicillin-resistant pneumococcal infections.

Keywords

sCRilecs-seq, mevalonate pathway, morphology, peptidoglycan synthesis, cell division, antibiotic resistance, amoxicillin, clomiphene, combination therapy

Introduction

Streptococcus pneumoniae (the pneumococcus) is an opportunistic human pathogen that is responsible for diseases such as pneumonia, middle ear infections, sepsis and meningitis[1-3]. *S. pneumoniae* is listed by the WHO as a priority pathogen for the development of novel antibiotics since it is one of the leading causes of fatal bacterial infections worldwide[1,2,4] and antibiotic resistance is on the rise[5-7]. The alarming increase in prevalence of penicillin non-susceptible *S. pneumoniae* was initially dealt with by the development and roll-out of the pneumococcal conjugate vaccines PCV7, PCV10 and PCV13 in 2001, 2009 and 2010, respectively[5]. These vaccines induce protection against infection caused by 7, 10 or 13 of the most prevalent serotypes of capsular polysaccharides that surround *S. pneumoniae*[3]. Since many of the targeted serotypes are associated with penicillin non-susceptibility, the occurrence of infections with such resistant strains decreased at first[5,8,9]. However, due to the high genomic plasticity of *S. pneumoniae*[10,11], serotype switching created penicillin non-susceptible escape mutants that are not covered by the currently available vaccines and that are once again gaining in prevalence[5,8].

Penicillin non-susceptible *S. pneumoniae* strains carry a variety of mutations in their penicillin binding proteins (PBPs) that decrease their affinity for penicillin and therefore increase resistance[4,7,12]. These mutations do not only lower the susceptibility to penicillin but also to other β-lactam antibiotics[13]. However, the efficacy of aminopenicillins such as amoxicillin is usually less affected by these mutations, meaning that amoxicillin remains a viable treatment option for many penicillin non-susceptible strains and therefore became one of the frontline antibiotics to treat pneumococcal infections[13-17]. However, highly penicillin resistant strains have been found to also be amoxicillin non-susceptible[5,6], thereby now also threatening the clinical efficacy of this widely used antibiotic.

Because of the rise in antibiotic resistance, we urgently need new antibiotic targets and/or need to find ways to extend the clinical efficacy of our current antibiotic arsenal. To contribute towards this goal, we developed sCRilecs-seq (subsets of CRISPR interference libraries extracted by fluorescence activated cell sorting coupled to next generation sequencing), a high-throughput single-cell based screening approach that we exploited to find targets that could resensitize resistant *S. pneumoniae* strains towards amoxicillin. sCRilecs-seq is based upon genome-wide gene silencing using CRISPR interference (CRISPRi), which makes use of a catalytically dead form of the Cas9 enzyme, called dCas9[18]. dCas9 is guided towards its target site in the DNA by the provided sgRNA but is unable to introduce double-stranded breaks. Instead, the dCas9 enzyme acts as a roadblock for RNA polymerase, thereby halting transcription[18-20]. CRISPRi gene silencing

72 not only affects the target gene but influences the expression of an entire transcriptional unit[18-22]. This
73 technology therefore works at the operon level and generates strong polar effects that need to be
74 considered. Despite this limitation, CRISPRi has proven to be a very powerful genetic tool to perform
75 genome-wide depletion screens in various bacteria[22-27]. In the sCRilecs-seq screen used here,
76 subpopulations that display a phenotype of interest are collected using Fluorescence Activated Cell
77 Sorting (FACS), as has previously been done in eukaryotic cells[28] and for bacterial transposon libraries[29].
78 The abundance of sgRNAs in the sorted fractions are then compared to a defined control population to
79 look for genetic factors involved in the phenotype of interest. This highly flexible screening approach
80 allowed us to identify targets that can be exploited in our fight against bacterial infections.
81
82 Our sCRilecs-seq results highlight the importance of the mevalonate pathway for maintaining proper cell
83 morphology in *S. pneumoniae*. The mevalonate pathway is the only pathway used by *S. pneumoniae* to
84 produce isoprenoids, a highly diverse class of organic molecules that are essential to all life on earth and
85 that function – among others – in processes such as cell wall synthesis, electron transport, membrane
86 stability and protein modification[30,31]. Our screen revealed that inhibition of the mevalonate pathway in
87 *S. pneumoniae* leads to extensive cell elongation. We demonstrate that this elongation is caused by
88 insufficient transport of cell wall precursors across the cell membrane due to a limitation in the production
89 of undecaprenyl phosphate (Und-P), the lipid carrier responsible for this process[32]. This shortage of
90 peptidoglycan precursors allows cell elongation to continue but causes a block in cell division, pointing
91 towards the existence of a threshold concentration of peptidoglycan precursors to trigger cell division.
92
93 Additionally, based on the mevalonate depletion phenotype characterized here, we successfully designed
94 a combination treatment strategy targeting *S. pneumoniae*. In this combination treatment strategy,
95 amoxicillin is potentiated by the simultaneous administration of clomiphene, a widely used FDA-approved
96 fertility drug that was shown to block Und-P production in *Staphylococcus aureus*[33]. This combination of
97 compounds is particularly powerful against amoxicillin-resistant *S. pneumoniae* strains, as it is capable of
98 resensitizing these strains to clinically-relevant concentrations of amoxicillin *in vitro*. Our findings could
99 therefore provide a useful starting point for the development of treatment strategies that are effective
100 against the rising amount of amoxicillin-resistant *S. pneumoniae* infections and could extend the clinical
101 efficacy of this important antibiotic.
102

103 **Results**

104 **Amoxicillin treated *S. pneumoniae* are elongated**

105 To identify new druggable pathways that could potentiate the antimicrobial activity of amoxicillin, we first
106 established the impact of amoxicillin on pneumococcal morphology and growth. We therefore performed
107 time-lapse microscopy of *S. pneumoniae* in the presence or absence of amoxicillin. As shown in Figure 1A-
108 B and Movie S1-2, amoxicillin-treated cells initially elongate before they lyse. Indeed, quantitative image
109 analysis confirmed that amoxicillin causes cell elongation (Figure 1C), while growth curves in the presence
110 of this antibiotic demonstrate that lysis occurs since OD values decrease at high amoxicillin concentrations
111 (Figure 1D). To demonstrate that cell elongation is specifically caused by amoxicillin and does not generally
112 occur upon antibiotic treatment, we also assessed cell lengths in the presence of the fluoroquinolone
113 ciprofloxacin. As expected, ciprofloxacin did not induce cell elongation[34] (Figure 1C). Because it was shown
114 that synergy between antimicrobial compounds is most often detected when they target the same
115 process[35], we hypothesized that targets whose inhibition would cause cell elongation, like amoxicillin,
116 could potentially reinforce the antibacterial effect of this antibiotic.

117

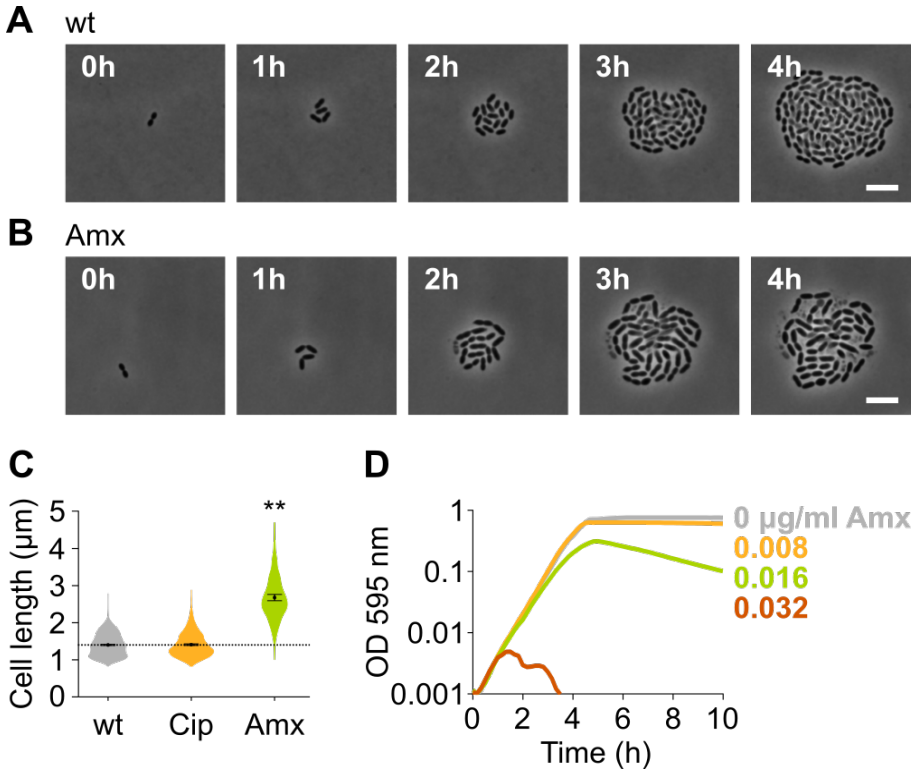

118

119 **Figure 1: Amoxicillin causes cell elongation before triggering cell lysis.** A) Snapshots of a time lapse analysis of *S. pneumoniae*
120 D39V growing in the absence of antibiotics (Movie S1). B) Snapshots of a time lapse analysis of *S. pneumoniae* D39V growing in
121 the presence of a sub-MIC concentration of amoxicillin (0.016 µg/ml) (Movie S2). C) The effect of sub-MIC concentrations of

122 ciprofloxacin (0.5 µg/ml) and amoxicillin (0.016 µg/ml) on the cell length of *S. pneumoniae* D39V was tested by phase contrast
123 microscopy. Quantitative analysis of micrographs shows that cell length increases upon treatment with amoxicillin. Data are
124 represented as violin plots with the mean ± SEM indicated, n ≥ 3, with each repeat containing >100 cells. Wilcox tests were
125 performed against wt without antibiotic as control group (dotted line) and p values were adjusted with an FDR correction; ** p <
126 0.01. More information on the statistics shown in panel C is provided in Figure S1 and Materials and Methods. D) *S. pneumoniae*
127 D39V was grown in the presence of different concentrations of amoxicillin and growth was followed by monitoring OD 595 nm.
128 Wt, wildtype; Cip, ciprofloxacin; Amx, amoxicillin.
129

130 **Development of sCRilecs-seq**

131 To identify pathways that lead to cell elongation upon inhibition, we developed a single-cell based, high-
132 throughput screening strategy where we combined CRISPRi gene silencing with high-throughput selection
133 of a phenotype of interest by Fluorescence Activated Cell Sorting (FACS). Using this approach, which we
134 call sCRilecs-seq, we screened for mutants that display an increase in forward scatter (FSC), which is a
135 rough indicator of cell size[36]. To facilitate downstream analyses, screening was performed in a *S.*
136 *pneumoniae* strain in which the DNA and the cell division protein FtsZ are marked. DNA was visualized
137 using the DNA-binding protein HlpA fused to GFP. HlpA, also known as HU, is a histone-like protein that
138 binds DNA aspecifically and is highly expressed in *S. pneumoniae*[37]. It is therefore often used as a nucleoid
139 marker[37,38]. FtsZ was marked by fusing it to mCherry. To this end, the native *hlpA* and *ftsZ* genes of *S.*
140 *pneumoniae* D39V were replaced by *hlpA-gfp* and *ftsZ-mCherry*, respectively. Both of these fusions were
141 previously shown to support viability[37,38]. Additionally, the gene encoding dCas9 was inserted into the
142 pneumococcal chromosome and was placed under tight control of an IPTG-inducible P_{lac} promoter[21,23].
143 The resulting strain (VL3117: D39V P_{lac}-*dcas9 hlpA-gfp ftsZ-mCherry*) was transformed with a pool of 1499
144 different integrative plasmids carrying constitutively-expressed sgRNAs that together target the entire
145 coding genome[23]. This way, we created a pooled CRISPRi library where each cell expresses a certain sgRNA
146 resulting in transcriptional downregulation of a specific gene or operon upon induction of dCas9 (Figure
147 2A).
148

149 We next grew the library in C+Y medium at 37°C for 3.5h in the presence of 1 mM IPTG to induce dCas9.
150 The pooled and induced library was subjected to FACS and different fractions of the population were
151 sorted (see Materials and Methods). Of note, *S. pneumoniae* grows as short cell chains[39] and the number
152 of cells present in a chain could influence the FSC read-out. To ensure that measurements were taken at
153 the single-cell level, chains were mechanically disrupted by vigorous vortexing before sorting took place.
154 We confirmed that this approach is successful at breaking up cell chains ensuring that morphology was

155 evaluated for single cells rather than entire chains (Figure S2A-C). Ten percent of the population with the
156 highest FSC values was collected. As a control, the centermost 70% of the population was sorted as well.
157 For both collected fractions, sgRNAs were amplified by PCR using primers that contain Illumina adapters
158 (see Materials and Methods). After sequencing, sgRNA read counts were compared between the sorted
159 fractions. This approach (Figure 2A) enabled us to identify sgRNAs that are significantly enriched in the
160 fraction of the population with highest FSC values. These sgRNAs point to genes or operons necessary to
161 maintain normal cell size.
162

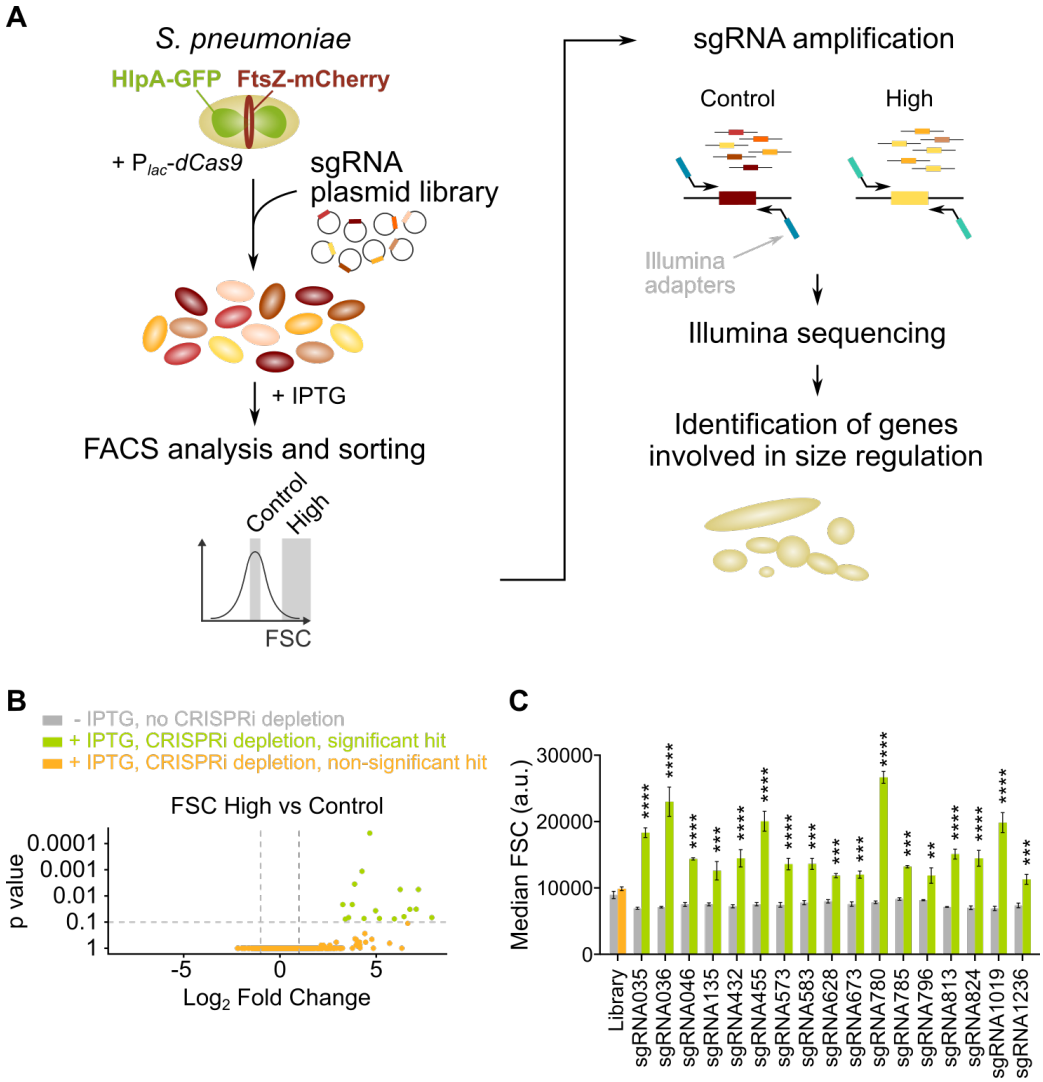

163
164 **Figure 2: sCRilecs-seq reliably identifies operons involved in cell size regulation.** A) A pooled CRISPRi library was constructed in
165 *S. pneumoniae* D39V P_{lac}-*dcas9 hlpA-gfp ftsZ-mCherry* (VL3117) by transformation of a plasmid library encoding 1499
166 constitutively-expressed sgRNAs that together target the entire genome. This CRISPRi library was grown in the presence of IPTG
167 for 3.5h to induce expression of dCas9, and cultures were sorted based on forward scatter (FSC) as a proxy for cell size. 10% of
168 the population with the highest FSC values was sorted, as well as the centermost 70% of the population which served as a control.

169 sgRNAs from sorted fractions were amplified by PCR using primers that contain Illumina adapters. Amplified sgRNAs were
170 sequenced and mapped to the *S. pneumoniae* genome. sgRNA read counts were compared between the different sorted fractions
171 to identify gene depletions that lead to increases in cell size. B) A volcano plot shows the statistical significance and enrichment
172 for every sgRNA in the fraction of the population with high FSC values compared to the control with normal FSC values. C)
173 Significant sgRNA hits were validated by studying individual mutants. Flow cytometry measurements of mutants grown with and
174 without IPTG were compared. Note that the entire CRISPRi library was also included in this experiment ('Library') as a control.
175 Data are represented as mean ± SEM, n = 3. ** $p < 0.01$, *** $p < 0.001$, **** $p < 0.0001$, t-test with Holm-Sidak correction for
176 multiple comparisons.
177
178 **sCRilecs-seq reliably identifies several targets involved in maintaining proper cell size**
179 Following this strategy, we were able to identify 17 sgRNAs that were significantly enriched in the fraction
180 of the population with high FSC values (Figure 2B, Figure S2D-E and Table S1), indicating that depletion of
181 these sgRNA targets leads to an increase in cell size. In a next step, we evaluated the reliability of our
182 sCRilecs-seq screen by validating these hits. The corresponding sgRNAs were individually cloned and
183 transformed to strain D39V P_{lac}-*dcas9 hlpA-gfp ftsZ-mCherry* (VL3117) and their effect was evaluated by
184 flow cytometry. The median FSC value for each depletion was recorded and compared to the median
185 value of the same strain without induction of dCas9. As shown in Figure 2C, all of the significant FSC hits
186 from the sCRilecs-seq screen demonstrated increased FSC levels upon depletion, meaning that no false
187 positives were identified and that this screen had a success rate of 100%.
188
189 The reliability of our screening approach is also reflected by the fact that many of the significant hits are
190 known to be involved in processes that influence cell size and/or morphology (Table S1). For example, 3
191 out of 17 hits are involved in cell division (i.e. *divIB*, *ftsL*, *ylmH*), 1 hit interferes with peptidoglycan
192 synthesis (*murF*) and at least 3 hits target the production of teichoic acids (*licD1*, *tacF*, *tacL*, and the operon
193 containing *tarQ*, *tarP* and *licD3*). These glycopolymers are an important component of the *S. pneumoniae*
194 cell envelope and are necessary to maintain proper cell morphology[21,40,41]. The fact that these hits are
195 picked up by our screen demonstrates that our strategy is capable of extracting biologically relevant
196 information.
197
198 Interestingly, when performing Gene Ontology (GO) enrichment[42-44] to look for biological processes that
199 are found among the hits more often than expected based on random chance, one biological process, i.e.
200 biosynthesis of isoprenoids, was found to be significantly overrepresented (Fold Enrichment = 56, P value
201 = 0.0019). We therefore decided to further focus on isoprenoid biosynthesis and how disturbances in this

202 process lead to changes in *S. pneumoniae* cell size that might be exploited as a novel antimicrobial
203 strategy.
204
205 **Depletion of mevalonate pathway components leads to cell elongation**
206 *S. pneumoniae* synthesizes isoprenoids through the mevalonate pathway[30,45]. This pathway, with
207 mevalonic acid (mevalonate) as intermediate, produces the C5 precursors, isopentenyl diphosphate and
208 dimethylallyl diphosphate (Figure 3A), which can be condensed into large and diverse isoprenoids[30]. In *S.*
209 *pneumoniae*, all proteins involved in the mevalonate pathway are encoded by two different operons[45,46],
210 both of which were identified as hits in our sCRilecs-seq screen. In a first step, we made clean, non-
211 CRISPRi-based deletion/complementation strains for both of these operons. In an *S. pneumoniae* D39V
212 strain that encodes the *hlpA-gfp* and *ftsZ-mCherry* fusion proteins (VL3404), the native mevalonate genes
213 were deleted and a complementation construct under control of the IPTG-inducible P_{lac} promoter was
214 inserted ectopically in the genome (Figure 3B). The resulting two deletion/complementation strains
215 (VL3565 and VL3567) were then used to assess the effect of mevalonate synthesis on cell size and growth.
216
217 Phase contrast microscopy on cells depleted for the mevalonate pathway operons demonstrated large
218 increases in cell length (Figure 3C-D and S3A-B), confirming the sCRilecs-seq screen. Even though cells also
219 became slightly wider upon mevalonate depletion (Figure 3C), cell length was disproportionally affected.
220 Cells attained more than twice their normal length when the mevalonate operons were depleted (Figure
221 3D and S3A) and the length/width ratio increased significantly (Figure S3B). In addition to cell elongation,
222 depletion of the mevalonate operons led to severe growth defects (Figure 3E). Importantly, the elongated
223 phenotype and observed growth defects could be complemented by ectopic induction of the mevalonate
224 operons with an optimized concentration of IPTG (Figure 3F-G and S3A), demonstrating that these
225 phenotypes are not due to polar effects of the mutations. Time lapse microscopy upon depletion of the
226 mevalonate operons confirmed these findings, showing that cells initially continue to grow and elongate
227 before lysis takes place (Figure 3J and Movie S3-4). Of note, these phenotypes were reproducible in
228 deletion/complementation strains that do not carry the *hlpA-gfp* and *ftsZ-mCherry* fusions (VL3708 and
229 VL3709) (Figure S3C-F).
230
231 Although the severe growth defects associated with depletion of the genes involved in mevalonate
232 biosynthesis point to the importance of this pathway for *S. pneumoniae* physiology, cultures were not
233 fully sterilized at late time points and many survivors remained (Figure 3E). To test whether the

234 mevalonate pathway is essential for *S. pneumoniae* viability and that the survival of the depletion strains
235 at late time points is due to leaky expression and/or suppressor mutations, we attempted to delete the
236 mevalonate operons without providing a complementation construct. As expected for essential genes, we
237 were unable to delete these operons. However, when mevalonic acid – an intermediary in the mevalonate
238 pathway (Figure 3A) – was added to the growth medium, we were able to delete operon 1, as was also
239 shown previously in *S. pneumoniae* and *S. aureus*[45,47-49]. As expected based on pathway architecture,
240 deleting operon 2 – which encodes proteins that work downstream of mevalonic acid – remained
241 impossible. We next grew *S. pneumoniae* Δ*operon 1* (VL3702) with different concentrations of mevalonic
242 acid. Cells grew normally and attained normal cell lengths when a high concentration of mevalonic acid
243 was added to the growth medium (Figure 3H-I). However, decreasing the concentration of mevalonic acid
244 led to cell elongation and growth defects that became more pronounced at lower concentrations, thereby
245 phenocopying genetic depletion of operon 1 and 2. In fact, when no mevalonic acid is provided at all,
246 cultures are driven to full extinction (Figure 3I). These results confirm that the mevalonate pathway is
247 essential for *S. pneumoniae* viability and that it is the only pathway through which this bacterium can
248 synthesize isoprenoids[45].
249

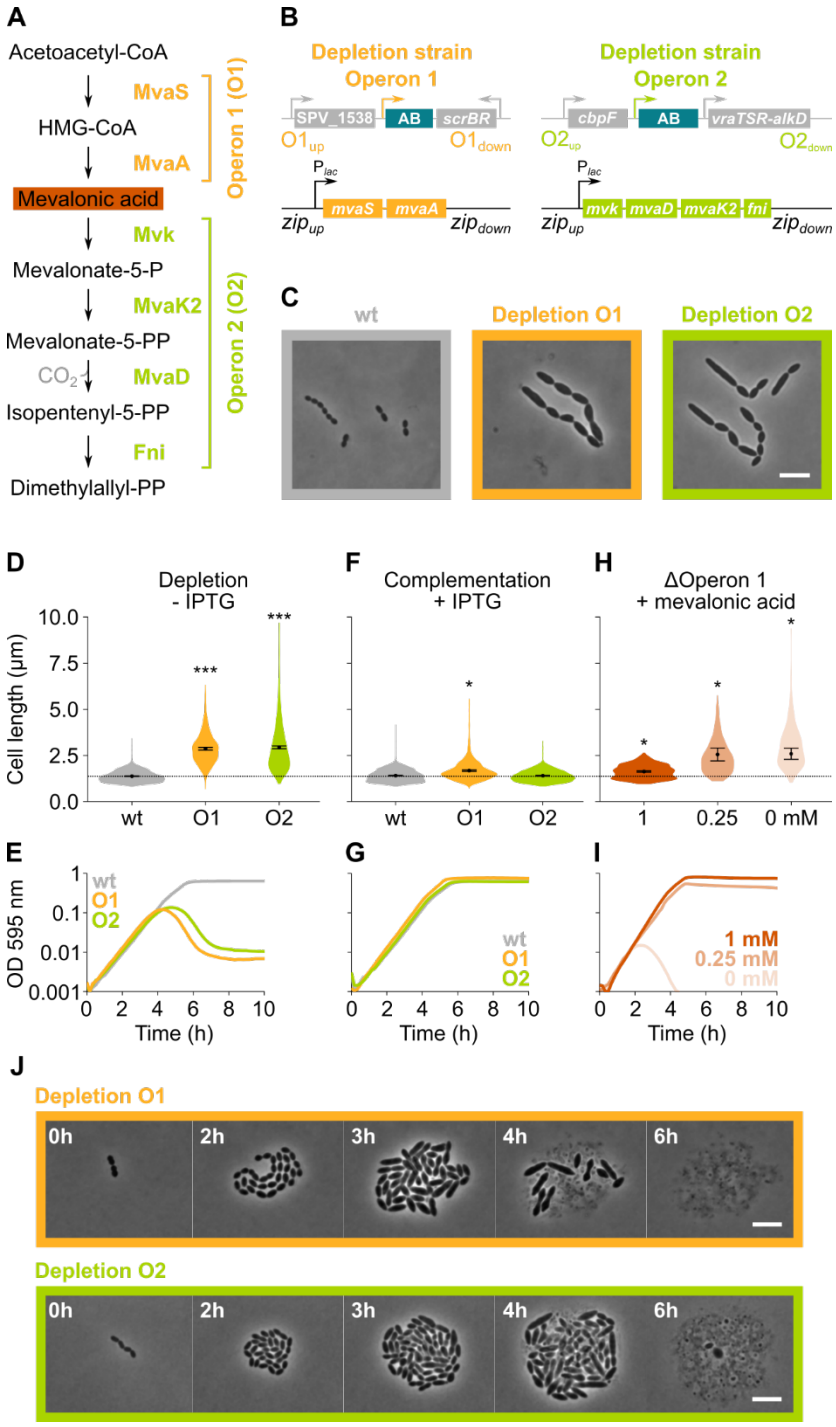

Figure 3: The mevalonate pathway is essential for *S. pneumoniae* and leads to cell elongation upon depletion. A) The mevalonate pathway and its genetic organization in *S. pneumoniae* is depicted. B) A genetic representation of the mevalonate depletion strains is shown. The native mevalonate operons were deleted and replaced by an antibiotic marker (AB) and a complementation construct under control of the P_{lac} promoter was inserted at the *zip* locus[50] in the *S. pneumoniae* genome. C) Phase contrast microscopy images of *S. pneumoniae* wt or upon depletion of one of the mevalonate operons for 4h in VL3565 and VL3567 are shown. Scale bar, 5 µm. D) Quantitative analysis of phase contrast micrographs shows that cell length increased when mevalonate operons were depleted. Data are represented as violin plots with the mean ± SEM indicated, n ≥ 3, with each

258 repeat containing > 100 cells. E) Depletion of mevalonate operons led to a severe growth defect. Data are represented as the
259 mean, n ≥ 3. F) The elongated phenotype upon depletion of mevalonate operons could be complemented by inducing their
260 expression with IPTG. Data are represented as violin plots with the mean ± SEM indicated, n ≥ 3, with each repeat containing >
261 100 cells. G) The growth defect associated with depletion of mevalonate operons could be fully complemented by inducing their
262 expression with IPTG. Data are represented as the mean, n ≥ 3. H) A mutant in which the first mevalonate operon was deleted
263 (VL3702, no complementation construct) displayed increased cell length when the concentration of mevalonic acid added to the
264 growth medium was decreased. Data are represented as violin plots with the mean ± SEM indicated, n ≥ 3, with each repeat
265 containing > 20 cells. I) Growing the mutant in which the first mevalonate operon is deleted (no complementation construct) with
266 decreasing concentrations of external mevalonic acid led to an increasing growth defect, resulting in full extinction of the culture
267 when no mevalonic acid was provided. Data are represented as the mean, n ≥ 3. J) Snapshot images of phase contrast time lapse
268 experiments with mutants in which the first or second mevalonate operon was depleted (VL3565 and VL3567) are shown. Strains
269 were grown on agarose pads of C+Y medium without the inducer IPTG. Scale bar, 5 µm. Wilcox tests were performed against wt
270 - IPTG as control group (dotted line) and p values were adjusted with an FDR correction; * $p < 0.05$, *** $p < 0.001$. More
271 information on the statistics shown in panel D, F and H is provided in Figure S3A and Materials and Methods.
272

273 **Depletion of mevalonate operons primarily interferes with cell division**

274 We next asked how depletion of mevalonate pathway components results in an elongated phenotype.
275 Microscopic investigation of mevalonate depleted cells showed that these bacteria contain a large
276 amount of unconstricted FtsZ rings (Figure 4A-B). High-resolution investigation of this phenotype by
277 Transmission Electron Microscopy (TEM) showed that depletion of the mevalonate operons resulted in
278 an unusually high occurrence of initiated septa that appear to be blocked for further constriction, whereas
279 division septa at all stages of constriction could be found in a wild-type strain (Figure 4C). The inability to
280 constrict and divide could explain the observed filamentation if cell elongation still occurs.
281

282 To investigate if indeed peripheral peptidoglycan synthesis remains active upon depletion of the
283 mevalonate operons, we labeled sites of active peptidoglycan synthesis with Fluorescent D-Amino Acids
284 (FDAAs)[51]. In a first pulse, cells were labeled with the green FDAA, sBADA, for 5 min and a second 5 min
285 pulse consisted of the red FDAA, RADA (see Materials and Methods). Fluorescence microscopy showed
286 that both peripheral and septal peptidoglycan synthesis occur in a wt strain (Figure 4D). Likewise, also the
287 mevalonate depletion strains showed sites of active peptidoglycan synthesis, indicating that not all cell
288 wall production is halted. However, in this case, we almost exclusively detected peripheral peptidoglycan
289 synthesis directed at cell elongation (Figure 4D). Indeed, when defining septal peptidoglycan synthesis as
290 FDAA bands that are less than 70% the maximal cell width (i.e. sites of constriction, a criterion also used
291 previously[52]), quantitative analysis of hundreds of peptidoglycan synthesis sites demonstrated that the
292 amount of septal synthesis is drastically reduced when transcription of the mevalonate operons is

293 repressed (Figure 4E). Additionally, it is clear that even though peripheral peptidoglycan synthesis
294 continues upon mevalonate depletion, this process is slowed down since FDAA intensity is decreased
295 under these conditions, indicating that less peptidoglycan is being produced (Figure 4D and F).
296
297 Taken together, these results strongly indicate that mevalonate depletion leads to filamentation because
298 cell division is blocked while peptidoglycan synthesis for cell elongation can still occur, albeit at a lower
299 rate. However, elongation does not continue indefinitely and cells eventually lyse (Figure 3J and Movie
300 S3-4). Since lysis usually occurs through weakening of the peptidoglycan cell wall[53], we hypothesize that
301 extended depletion of mevalonate operons eventually affects the integrity and/or rigidity of the
302 peptidoglycan mesh, leading to cell lysis. However, considering the initial phenotypes found, we conclude
303 that the primary effect of mevalonate depletion is a block in septal peptidoglycan synthesis necessary for
304 cell division.
305

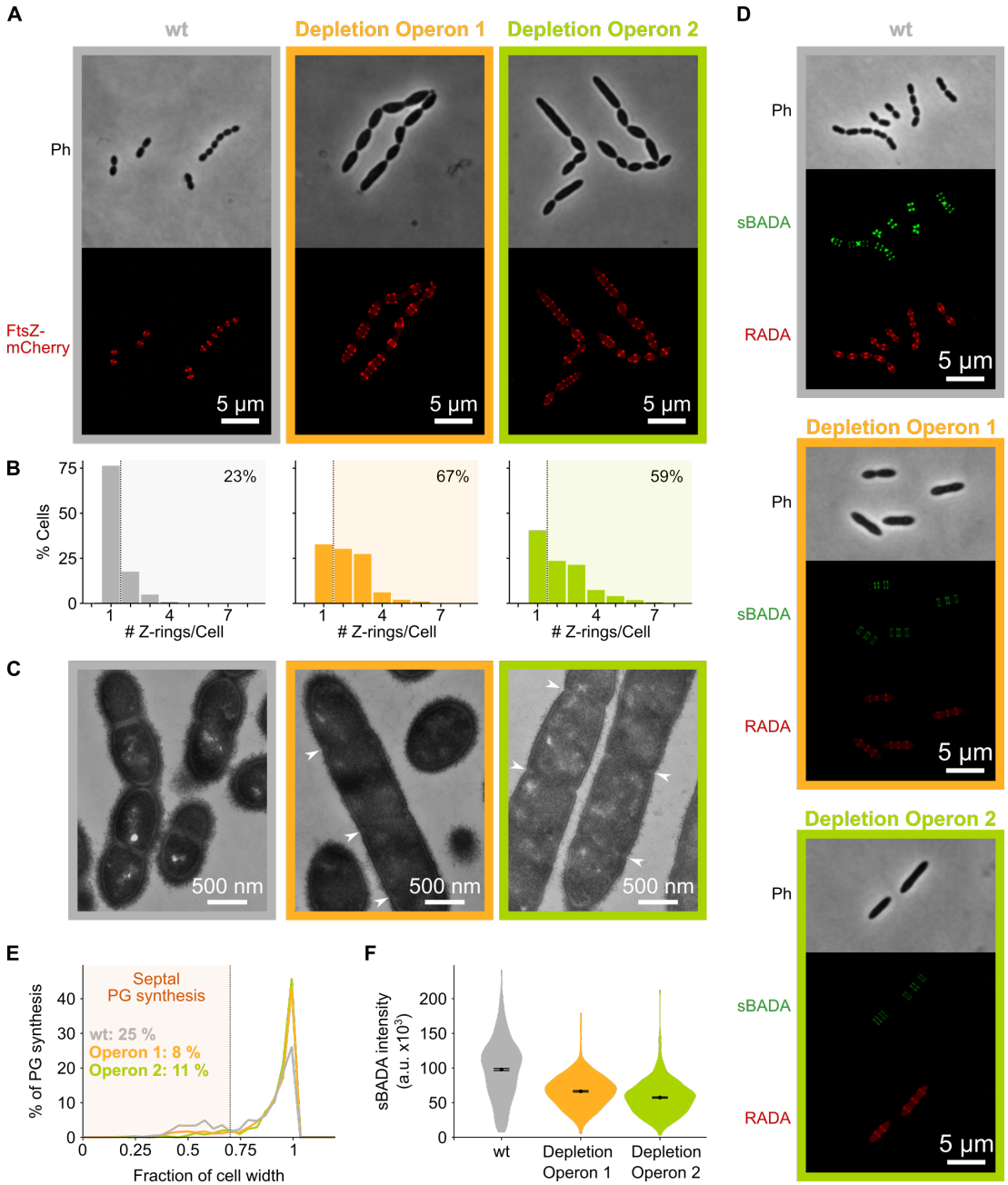

Figure 4: Depletion of mevalonate operons prevents cell division. A) While *S. pneumoniae* wt cells typically contain one FtsZ-mCherry ring at the cell center, depletion of either one of the mevalonate operons led to strongly elongated cells with multiple unconstricted FtsZ rings. Images were obtained using strains VL3404, VL3565 and VL3567 that encode the *ftsZ-mCherry* fusion. B) Quantitative analysis of microscopy pictures was used to determine the number of Z-rings per cell. Pictures from at least 6 independent repeats were analyzed, each including over 100 cells. C) Transmission Electron Microscopy (TEM) images show that elongated cells contained many initiated septa that appear to be blocked in further progression of constriction (white arrow heads). Images were obtained using strains VL333, VL3708 and VL3709 that do not encode fluorescent fusion proteins. D) Pulse labeling *S. pneumoniae* with the green FDAA, sBADA, and 15 min later with the red RADA shows sites of active peptidoglycan synthesis involved in either elongation or constriction. Images were obtained using strains VL333, VL3708 and VL3709 that do

316 not encode fluorescent fusion proteins. E-F) Quantitative image analysis of sites of active peptidoglycan synthesis labeled with
317 FDAAs shows that depletion of mevalonate operons eliminated septal peptidoglycan synthesis since virtually no narrow sBADA
318 or RADA bands can be found (E) and that the intensity of FDAA labeling decreased upon mevalonate depletion, indicating that
319 peripheral peptidoglycan synthesis was slowed down (F). Number of sBADA and RADA bands analyzed for each condition > 400.
320

321 **Depletion of mevalonate operons prevents cell division by limiting the export of peptidoglycan**
322 **precursors**

323 The mevalonate pathway provides the precursor for the production of all isoprenoids in *S.*
324 *pneumoniae*[30,45]. Thus, a shortage in the production of any of these isoprenoids could underlie the
325 phenotypic effects of perturbed mevalonate production. However, given the nature of the observed
326 phenotype, we thought it most likely that a shortage in the production of undecaprenyl phosphate (Und-
327 P) would be responsible for the observed effects. Und-P is a C55 isoprenoid that acts as the lipid carrier
328 for transport of cell envelope precursors from the cytoplasm to the extracellular environment[32]. Und-P is
329 produced by the dephosphorylation of undecaprenyl pyrophosphate (Und-PP), which is in turn
330 synthesized by UppS (undecaprenyl pyrophosphate synthase) by the addition of 8 isopentenyl units to the
331 C15 isoprenoid farnesyl-PP[30,32] (Figure 5A). To test whether the observed effects of mevalonate depletion
332 are indeed caused by a deficiency of Und-P, we constructed a *uppS* deletion/complementation strain
333 (VL3584, Figure 5B). When this strain was grown in absence of *uppS* expression, cells were elongated and
334 growth was reduced (Figure 5C-D), thereby phenocopying mevalonate operon mutants. In addition, UppS
335 depleted cells contained multiple unconstricted Z-rings and initiated septa that failed to constrict further,
336 even though peripheral peptidoglycan synthesis still occurred as demonstrated by TEM and fluorescence
337 microscopy (Figure 5D-F). Note that *uppS* was not identified by our sCRilecs-seq screen, likely because it
338 is in an operon with several other essential genes not directly involved in cell division, such as *cdsA* and
339 *proS*[46]. We thus conclude that the negative effects caused by depletion of the mevalonate operons can be
340 explained by insufficient production of Und-PP and subsequently Und-P.
341

342 The isoprenoid Und-P carries precursors of the capsule, teichoic acids and peptidoglycan across the
343 membrane[32]. The observed phenotype of mevalonate and *uppS* mutants could therefore be caused by a
344 shortage in either one or a combination of these components. To test which of these pathways contribute
345 to the observed phenotypes upon mevalonate depletion, we tested each of them individually. First, we
346 deleted the *cps* operon responsible for capsule synthesis in our D39V strain[54]. As shown in Figure S4A-B,
347 *cps* mutant cells were not elongated nor was growth rate affected, demonstrating that a shortage of
348 capsule synthesis does not contribute to the mevalonate depletion phenotype. Next, we focused on the

349 possible contribution of both teichoic acid and peptidoglycan synthesis by depleting the enzymes
350 responsible for coupling the final cytoplasmic precursors to Und-P before transport to the outside of the
351 cell. For peptidoglycan, it is known that the MurNAc-pentapeptide moiety that is produced in the
352 cytoplasm is coupled to Und-P by MraY[32]. Based on sequence similarity, bioinformatic analysis indicated
353 that the enzyme that does the same for teichoic acid precursors in *S. pneumoniae* is SPV_1620[55].
354 Deletion/complementation strains for these genes were created and the effect of depletion of either
355 MraY or SPV_1620 was assessed (strain VL3585 and VL3586, respectively). Surprisingly, depletion of
356 neither MraY nor SPV_1620 produced cell morphologies that resembled mevalonate operon depletions
357 at the time we usually assess them (Figure 5G-H, time point 4h). However, since at this time cells were
358 severely malformed and many had already lysed, we decided to follow these depletions through time and
359 also record morphologies at earlier time points. Figure 5G shows the progression of these depletions in
360 terms of average cell length, while Figure 5H shows representative morphologies. From this analysis it
361 became clear that – although depletion of both MraY and SPV_1620 led to increased cell length – the
362 phenotype obtained upon SPV_1620 depletion differed profoundly from the phenotypes found when
363 depleting mevalonate operons. Depletion of MraY, on the other hand, was highly similar to the
364 mevalonate phenotype at early time points. We thus conclude that a deficiency in the export of
365 peptidoglycan precursors is mainly responsible for the elongated phenotype that is observed when
366 components of the mevalonate pathway are depleted. Since we previously showed that this elongated
367 phenotype is caused by continued peripheral peptidoglycan synthesis while septum synthesis does not
368 occur, it appears as though a certain threshold level of peptidoglycan precursors is needed for cells to
369 divide. Cell elongation, on the other hand, can proceed even with a lower amount of peptidoglycan
370 precursors indicating switch-like behavior between the two peptidoglycan growth modes[40].
371

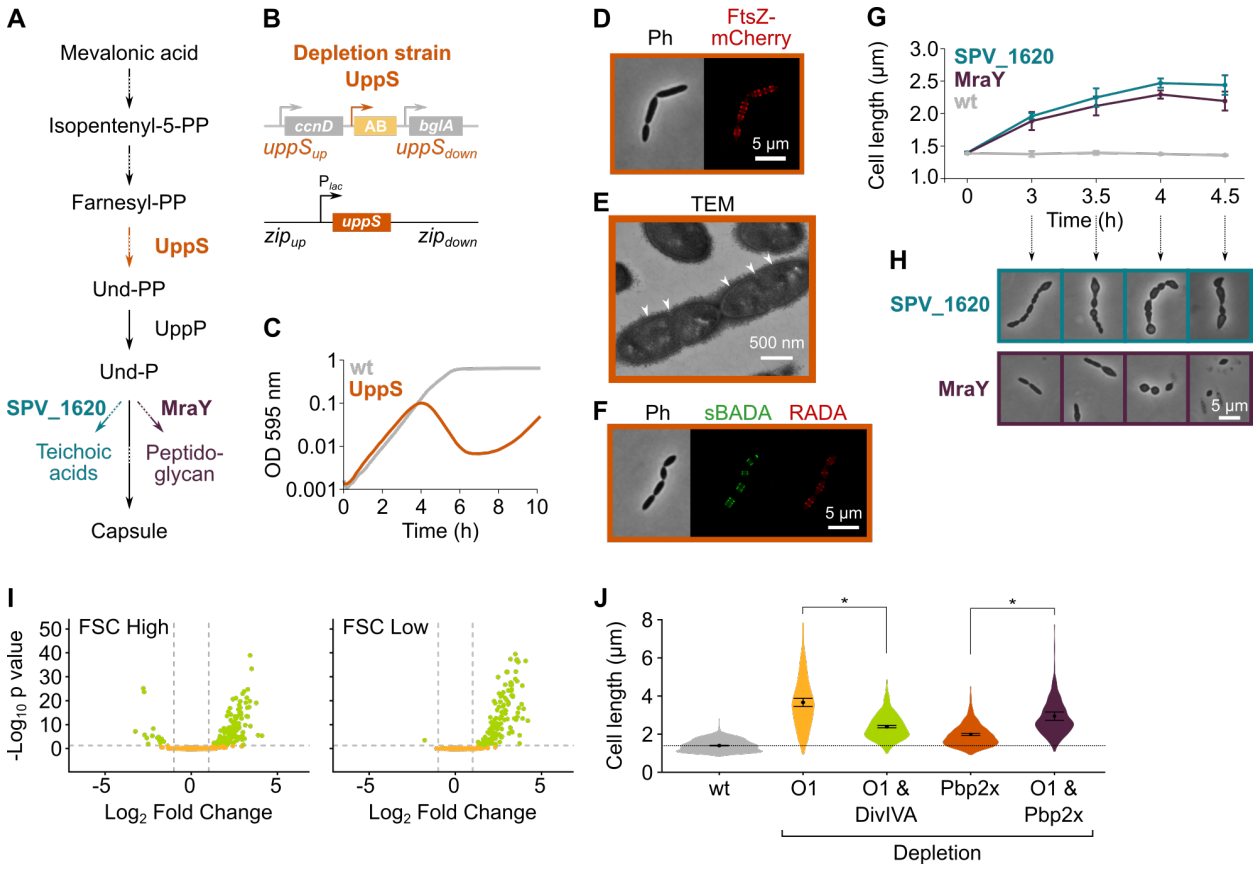

Figure 5: Depletion of the mevalonate pathway prevents cell division by limiting the export of peptidoglycan precursors which preferentially inhibits cell division. A) After conversion of mevalonic acid into the basic isoprenoid building block isopentenyl-5-PP in the mevalonate pathway, this building block is condensed into the C15 molecule Farnesyl-PP. Farnesyl-PP can be used by UppS for the production of undecaprenyl pyrophosphate (Und-PP), which after dephosphorylation to Und-P by UppP acts as the lipid carrier for the transport of precursors of peptidoglycan, the capsule and teichoic acids across the cell membrane. B) A genetic overview of the UppS depletion strains is shown. The native *uppS* gene was replaced by an antibiotic marker (AB) and a complementation construct under control of the P_{lac} promoter was inserted at the *zip* locus in the *S. pneumoniae* genome. C) Depletion of UppS in VL3584 caused a growth defect similar to depletion of the mevalonate operons. We confirmed that the growth observed after an initial phase of lysis was due to suppressor mutants that are no longer sensitive to UppS depletion (Figure S4C). Data are represented as averages, n ≥ 3. D) Like depletion of the mevalonate operons, depletion of UppS caused an elongated phenotype where cells contained multiple unconstricted FtsZ rings. Images were obtained using strain VL3585 which encodes *ftsZ-mCherry*. E) Transmission Electron Microscopy (TEM) images show that cells elongated due to UppS depletion contained many initiated septa that appeared to be blocked in further progression of constriction (white arrow heads). Images were obtained using strain VL3710 that does not encode fluorescent fusion proteins. F) Pulse labeling *S. pneumoniae* depleted for UppS with the green FDAA, sBADA, and subsequently with the red RADA dye showed sites of active peptidoglycan synthesis, which are in this case all directed at cell elongation. Images were obtained using strain VL3710 that does not encode fluorescent fusion proteins. G) The effect of the depletion of MraY and SPV_1620 on cell length was followed through time using quantitative image analysis. For each biological repeat (n ≥ 3), more than 50 cells were used to calculate the average cell length. Data are represented as the mean ± SEM of these averages. H) Representative morphologies of VL3585 and VL3586 corresponding to the

392 analysis from panel G are shown. I) A pooled CRISPRi library was constructed in VL3834 (*S. pneumoniae* D39V P_{lac}-*dCas9* Δ*mvaA*-
393 *mvaS*). This CRISPRi library was grown in the presence of the dCas9 inducer, IPTG, and limiting amounts of mevalonic acid (100
394 µM). Cultures were sorted based on cell size (FSC); 10% of the population with the highest and lowest values were sorted, as well
395 as the centermost 70% of the population which served as a control. sgRNAs from the sorted fractions were sequenced and read
396 counts were compared to identify gene depletions that led to changes in cell size. Volcano plots show the statistical significance
397 and enrichment for every sgRNA in the fraction with high FSC values (FSC High) and low FSC values (FSC Low) compared to the
398 control. J) Quantitative analysis of microscopy images shows the changes in cell length upon single or double depletions of the
399 first mevalonate operon (O1, *mvaS*-*mvaA*), DivIVA or Pbp2x. Data are represented as violin plots with the mean ± SEM indicated,
400 $n \geq 3$, with each repeat containing > 90 cells except for the double O1 Pbp2x depletion where not enough surviving cells could be
401 visualized and the threshold was put at 10 cells. Wilcox tests were performed and p values were adjusted with an FDR correction;
402 * $p < 0.05$.
403

404 **A sCRilecs-seq screen on mevalonate depleted cells to study the underlying genetic network**

405 To identify pathways and genes that are particularly sensitive to reduced mevalonate levels, and to obtain
406 clues on why a lowered concentration of extracellular peptidoglycan precursors would allow elongation
407 but not division, we performed a second sCRilecs-seq screen based on cell size (FSC) in a genetic
408 background in which the first mevalonate operon was deleted (VL3834: D39V P_{lac}-*dcas9* Δ*mvaS*-*mvaA*).
409 This way, we could look for gene depletions that aggravate the observed phenotype, i.e. make cells even
410 longer, and depletions that compensate for the mevalonate-dependent cell elongation. During
411 construction of this CRISPRi library and prior to selection, cultures were grown in the presence of a high
412 concentration of mevalonic acid (1 mM) which ensures wild-type growth and normal cell size even though
413 the first mevalonate operon is deleted (see Figure 3H-I). After construction of the pooled CRISPRi library,
414 cultures were grown with limiting amounts of external mevalonic acid (100 µm) to trigger the elongated
415 phenotype caused by mevalonate deficiency (Figure S5A). Simultaneously, dCas9 expression was induced
416 by the addition of 1 mM IPTG for 3.5h. 10% of the population with the highest and lowest FSC values were
417 sorted by FACS and the centermost 70% of the population was collected to serve as a control. Comparing
418 sgRNA read counts from the collected fractions led to the identification of many significantly enriched
419 targets in the populations with the highest and lowest FSC values (Figure 5I, Figure S5B and Table S2).
420

421 GO enrichment analysis identified cell division and closely related GO categories as significantly
422 overrepresented in elongated cells (Table S3). This suggests that depleting genes involved in cell division
423 will lead to additional cell elongation upon mevalonate depletion. On the other hand, sgRNAs that are
424 enriched in the small fraction of the population are often involved in protein expression (transcription,
425 translation, ribosome assembly, etc.) or energy metabolism. Halting or interfering with protein expression

426 or energy production therefore appears to reduce cell elongation caused by mevalonate deficiency. The
427 results of these high-level analyses are clear; directly interfering with cell division reinforces the division
428 block imposed by mevalonate depletion and inhibiting protein expression or energy production, both of
429 which are necessary for growth in general, prevents cell elongation.
430
431 Additionally, when looking at individual genes and operons found among the significantly enriched hits,
432 some interesting patterns emerge. For example, the sgRNA targeting *divIVA* was strongly depleted from
433 the large fraction of the population and also highly enriched in the small fraction, indicating that the
434 depletion of DivIVA hampers cell elongation upon mevalonate depletion. DivIVA activity was previously
435 shown to be necessary for cell elongation and DivIVA is known to be phosphorylated by the
436 serine/threonine kinase StkP that is thought to constitute a molecular switch that governs elongation and
437 division[40,56-59]. Indeed, we confirmed that a double depletion of the first mevalonate operon and DivIVA
438 leads to reduced cell lengths in comparison to the depletion of mevalonate alone (Figure 5J), indicating
439 that also upon mevalonate depletion DivIVA activity assists cell elongation. However, cells depleted for
440 both mevalonate and DivIVA are still larger than wild-type cells, indicating that a limited amount of
441 elongation still occurs. Peripheral peptidoglycan synthesis enforced by mevalonate depletion is therefore
442 not fully dependent on DivIVA activity. Additionally, CRISPRi depletion of the SEDS proteins FtsW and RodA
443 had opposite effects on cell size in our screen (Table S2). These proteins are thought to be the primary
444 transglycosylases responsible for peptidoglycan polymerization during cell division and cell elongation,
445 respectively[60-63]. Moreover, CRISPRi depletion of Pbp2b, the transpeptidase that works in conjunction with
446 RodA to perform peripheral peptidoglycan synthesis[40,63,64], showed up in the shorter cell fraction (Table
447 S2). These results are in line with the hypothesis that cell elongation in mevalonate depleted cells is caused
448 by ongoing peripheral peptidoglycan synthesis while septal synthesis is inhibited. If this is true, then
449 depletion of Pbp2x, the essential pneumococcal PBP required for cell division and the prime target of the
450 penicillins including amoxicillin[65], should show a synthetic effect upon mevalonate depletion. As *pbp2x* is
451 located in an operon together with *mraY*, this could not be directly assessed in the sCRilecs-seq screen.
452 Therefore, we constructed a clean *pbp2x* depletion strain. As shown in Figure 5J, depletion of Pbp2x
453 indeed led to an increase in cell length and this phenotype was augmented under low mevalonate levels.
454
455 **The mevalonate pathway as druggable target in *S. pneumoniae***
456 Our results so far demonstrate that depletion of the mevalonate pathway leads to cell elongation due to
457 limited septal PG synthesis and these morphological effects can be enhanced by targeting other cell

458 division pathways. Since amoxicillin also causes elongation in *S. pneumoniae*, we set out to design a
459 combination treatment strategy using amoxicillin and exploiting the mevalonate depletion phenotype
460 characterized here. In a first step, we confirmed that the antibacterial effect of amoxicillin – but not that
461 of the fluoroquinolone ciprofloxacin – is increased upon mevalonate depletion, since amoxicillin could
462 inhibit growth already at sub-MIC concentrations when mevalonate became limiting (Figure S6A-B). These
463 results demonstrate that, in principle, it is possible to design a treatment strategy in which amoxicillin is
464 potentiated by targeting the mevalonate pathway.
465
466 In a second step, we looked for chemical compounds that could block either the mevalonate pathway or
467 the downstream production of Und-P. Three compounds were selected; simvastatin and farnesol are
468 expected to block the HMG-CoA reductase MvaA that catalyzes one of the first steps of the mevalonate
469 pathway[66-68], while clomiphene was shown to inhibit UppS in *S. aureus*[33]. To confirm the specificity of
470 these compounds for the mevalonate pathway or downstream production of Und-P, we first tested
471 whether they could induce the expected cell elongation in *S. pneumoniae*. Since only the addition of
472 clomiphene resulted in filamentation under our conditions (Figure 6A and S6D), we selected this
473 compound for further testing. Indeed, time lapse analysis showed considerable cell elongation in the
474 presence of clomiphene (Figure 6B and Movie S5). Moreover, clomiphene most likely targets the
475 production of Und-P, since sub-MIC concentrations of clomiphene led to severe growth defects in cultures
476 that were slightly depleted for mevalonate (Figure S6C).
477
478 We next combined clomiphene with either amoxicillin or ciprofloxacin at several different concentrations
479 and monitored the growth of an *S. pneumoniae* D39V wild-type strain by measuring OD. The success of
480 growth was quantified by calculating the area under the curve for a growth period of 10 hours. As can be
481 seen in Figure 6C, clomiphene did not affect the efficacy of ciprofloxacin. However, for amoxicillin,
482 potentiation by clomiphene was observed (Figure 6D). This is consistent with time lapse analyses that
483 show that survival of *S. pneumoniae* was much more affected when both compounds were combined
484 (Figure 6E and Movie S6). Indeed, in the presence of clomiphene, the concentration of amoxicillin
485 necessary to block pneumococcal growth decreased by a factor 2 to 8 (Table 1).
486
487 **Resensitizing antibiotic-resistant *S. pneumoniae* strains using clomiphene**
488 We next tested whether the potentiation by clomiphene is also present in clinically-relevant amoxicillin-
489 resistant *S. pneumoniae*. We therefore assessed the growth of a panel of resistant strains in the presence

490 of different concentrations of amoxicillin and clomiphene. The strains we tested are clinical isolates of
491 strains 19F, Spain-23F and 11A[5,69]. Results are presented in Figure 6F-H and Table 1 and show that
492 clomiphene potentiated the antimicrobial activity of amoxicillin also against clinical resistant strains.
493 Moreover, the potentiation was even stronger in these resistant genetic backgrounds. Indeed, the
494 concentration of amoxicillin necessary to block growth of these resistant strains decreased by a factor 16
495 to 64 in the presence of 8 µg/ml of clomiphene (Table 1), thereby reducing resistance below the EUCAST
496 clinical breakpoint for sensitivity (0.5 µg/ml)[70]. Our rationally designed combination treatment strategy
497 can thus resensitize amoxicillin-resistant *S. pneumoniae* strains so that they once again become fully
498 susceptible to amoxicillin *in vitro*. This treatment strategy could therefore prove useful in the fight against
499 amoxicillin-resistant *S. pneumoniae* infections.
500

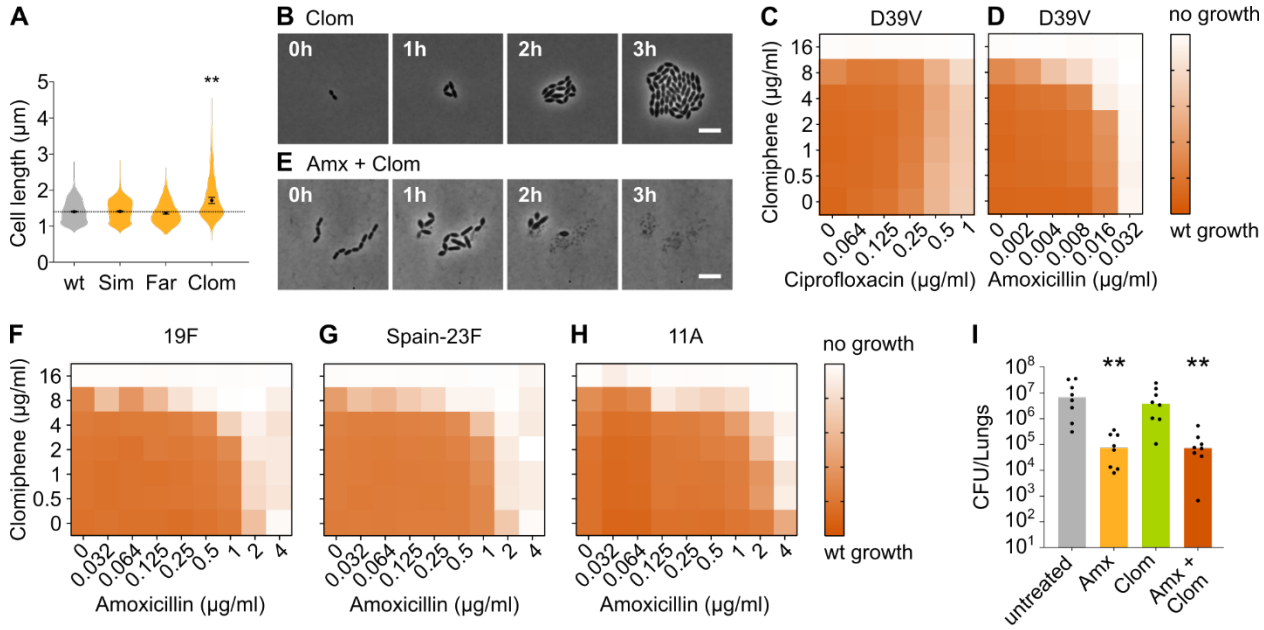

501

502 **Figure 6: Clomiphene, an inhibitor of Und-P production, potentiates amoxicillin.** A) The effect of several potential inhibitors of
503 Und-P production on the cell length of *S. pneumoniae* D39V (VL333) was tested (Sim 4 µg/ml, Far 4 µg/ml, Clom 8 µg/ml).
504 Quantitative analysis of microscopy images shows that cell length increased upon treatment with clomiphene. Data are
505 represented as violin plots with the mean ± SEM indicated, n ≥ 3, with each repeat containing > 100 cells. Wilcox tests were
506 performed against wt without treatment as control group (dotted line) and p values were adjusted with an FDR correction; ** p
507 < 0.01. More information on the statistics shown in panel A is provided in Figure S6D and Materials and Methods. B) Snapshot
508 images of phase contrast time lapse microscopy of *S. pneumoniae* D39V (VL333) in the presence of clomiphene (8 µg/ml). Scale
509 bar, 5 µm. C-D) OD_{595nm} growth curves were constructed for *S. pneumoniae* D39V (VL333) in the presence of different
510 concentrations of clomiphene and ciprofloxacin (C) or amoxicillin (D). Heatmaps of the area under the resulting growth curves
511 are shown. Number of biological repeats for all experiments, n ≥ 3. E) Snapshot images of phase contrast time lapse microscopy
512 of *S. pneumoniae* D39V (VL333) in the presence of clomiphene (8 µg/ml) and amoxicillin (0.016 µg/ml). Scale bar, 5 µm. F-H)

513 OD_{595nm} growth curves were constructed for *S. pneumoniae* 19F (F), Spain-23F (G) and 11A (H) in the presence of different
514 concentrations of clomiphene and amoxicillin. Heatmaps of the area under the resulting growth curves are shown. Number of
515 biological repeats for all experiments, n ≥ 3. I) The effect of the combination treatment with amoxicillin and clomiphene was
516 tested *in vivo* using a pneumonia superinfection model with a clinical isolate of *S. pneumoniae* serotype 19F. Mice (n=8 per group)
517 were infected intranasally first with H3N2 virus and then 7 days later with pneumococcus 19F. Mice were treated at 8 h and 12h
518 with clomiphene, amoxicillin, combination of both, or left untreated. Lungs were collected 24 h post-infection to measure the
519 bacterial load. CFU counts for individual mice are shown, and the bars represent the median value. The data were compared in a
520 Kruskall-Wallis test (One-Way ANOVA), ** $p < 0.01$. Wt, wildtype; Sim, simvastatin; Far, farnesol; Clom, clomiphene; Amx,
521 amoxicillin.
522
523 **Table 1: MIC values for amoxicillin/clomiphene and ciprofloxacin/clomiphene drug combinations (µg/ml).**

	Clomiphene		
	0 µg/ml	4 µg/ml	8 µg/ml
S. pneumoniae D39V			
Ciprofloxacin	1	1	1
Amoxicillin	0.032	0.016	0.004
S. pneumoniae 19F			
Amoxicillin	2	1	0.125
S. pneumoniae Spain-23F			
Amoxicillin	2	1	0.032
S. pneumoniae 11A			
Amoxicillin	4	2	0.125

524
525
526 We next tested whether this treatment strategy would prove useful in an *in vivo* setting, using a murine
527 pneumonia disease model (see Materials and Methods)[71]. Mice were infected on day 1 with influenza A
528 virus and superinfected on day 7 with *S. pneumoniae* 19F. Animals were treated with 5 mg of clomiphene
529 and/or 1 mg of amoxicillin at 8 and 12 hours post-pneumococcal infection, respectively. Twenty-four
530 hours post infection, the bacterial load in the lung was determined. Whereas treatment with amoxicillin
531 alone significantly lowered bacterial counts, administering only clomiphene did not influence the bacterial
532 load (Figure 6I). Treating mice with both clomiphene and amoxicillin did not show a stronger effect than
533 treatment with amoxicillin alone, meaning that the potentiation of amoxicillin we observed *in vitro* could
534 not be detected *in vivo* (Figure 6I). The same was true for CFU counts in the spleen (Figure S6E). To figure
535 out why our combination treatment strategy was not effective *in vivo*, we tried to estimate the active
536 concentration of clomiphene in the lung. Our *in vitro* tests showed that potentiation occurs at
537 concentrations of clomiphene of 4 µg/ml and higher, but these concentrations might not be achieved *in*

538 *vivo*. We therefore tested the growth of *S. pneumoniae* D39V *in vitro* in the presence of bronchoalveolar
539 lavage (BAL) fluid collected from mice treated with clomiphene. This experiment indicated that the active
540 concentration of clomiphene in the lung was lower than 4 µg/ml, which could explain the absence of
541 amoxicillin potentiation (Figure S6F).
542
543 **Discussion**
544 Here, we rationally designed a combination treatment strategy that resensitizes resistant *S. pneumoniae*
545 strains towards clinically relevant concentrations of amoxicillin, one of the most widely used antibiotics
546 to fight this human opportunistic pathogen[15-17]. By combining amoxicillin with the FDA-approved fertility
547 drug clomiphene[72-74], we were able to reduce amoxicillin MIC values of resistant strains 16 to 64-fold *in*
548 *vitro*, thereby decreasing them below the EUCAST clinical breakpoint for sensitivity.
549
550 **sCRilecs-seq reliably identifies several targets that regulate *S. pneumoniae* cell size**
551 This combination treatment strategy was based on the results of the sCRilecs-seq screen developed here.
552 sCRilecs-seq is a high-throughput single-cell-based screening approach that relies on genome-wide
553 CRISPRi depletion combined with sorting of cells that display a phenotype of interest. We here screened
554 for CRISPRi gene depletions that, like amoxicillin treatment, result in cell elongation. The rationale behind
555 this strategy is that synergy is most often detected between compounds that target the same process[35].
556 Although we used the sCRilecs-seq method to screen for increases in cell size, this approach could easily
557 be adapted to asses any phenotype of interest that can be measured by flow cytometry. In contrast to
558 'classic' CRISPRi-seq screens[22-27], our approach is therefore not limited to measuring changes in fitness but
559 can be used to evaluate a wide array of different phenotypes. Moreover, we show that sCRilecs-seq is
560 highly reliable and does not generate many false positive hits. In fact, in our screen, a success rate of 100%
561 was achieved. Interestingly, significant hits include a number of genes of unknown function that we can
562 now implicate in the maintenance of proper cell size. Our sCRilecs-seq approach is thus able to uncover
563 novel gene functions and can help to expand knowledge on any process of interest that can be evaluated
564 using flow cytometry.
565
566 **Depletion of mevalonate pathway genes leads to cell elongation through inhibition of cell division**
567 The sCRilecs-seq screen performed here revealed an important role for the mevalonate pathway in
568 maintaining proper cell size. Indeed, depletion of the genes involved in this pathway led to a very strong
569 increase in cell length. We have established that this cell elongation is due to a deficiency in the production

570 of Und-P, the lipid carrier that translocates all different cell envelope precursors across the cell
571 membrane[32], and subsequent limitation of the amount of peptidoglycan building blocks that is being
572 transported. The limiting amount of peptidoglycan precursors available for cell wall synthesis led to an
573 interesting phenotype. Whereas the peptidoglycan synthesis rate in general decreased, peripheral
574 peptidoglycan synthesis for cell elongation continued long after septal peptidoglycan synthesis for cell
575 division was inhibited. This observation points towards a difference in affinity and/or regulation of both
576 modes of peptidoglycan synthesis, where it appears that a certain threshold concentration of
577 peptidoglycan precursors needs to be exceeded in order for cell division to take place. Two potential
578 explanations for this observation can be put forward. First, it is possible that peptidoglycan synthesis
579 enzymes dedicated to cell division have a lower affinity for peptidoglycan precursors than their
580 counterparts that function in cell elongation. When cell wall precursors become limiting, the enzymes
581 involved in septal peptidoglycan synthesis would be outcompeted and cell division would cease while
582 elongation still occurs. On the other hand, it has previously been suggested that a more complex
583 regulatory mechanism decides whether cells elongate or divide. The serine/threonine kinase StkP and its
584 cognate phosphatase PhpP were suggested to constitute a molecular switch that coordinates septal and
585 peripheral peptidoglycan synthesis through phosphorylation and dephosphorylation of its targets[40,56-58].
586 Moreover, since StkP contains PASTA domains that are known to bind peptidoglycan precursors[40,56,57,75],
587 it has been suggested that StkP activity is regulated in response to the concentration of peptidoglycan
588 building blocks present[40,56,57]. We here indeed present evidence that the activity of both modes of cell wall
589 synthesis depends on the amount of peptidoglycan precursors that is exported. However, it was
590 previously shown that even though PASTA domains are necessary for StkP activation, peptidoglycan
591 binding is not required[75]. Moreover, the depletion of DivIVA upon reduced mevalonate conditions still
592 allowed a modest amount of cell elongation to occur. Since DivIVA is thought to be an important part of
593 the molecular switch between elongation and division instigated by StkP[58,59], it appears as though
594 elongation upon mevalonate depletion is at least partially independent of this molecular switch.
595 Therefore, further research will be necessary to determine why elongation is favored over division when
596 peptidoglycan precursors become limiting.
597
598 **Inhibition of Und-P synthesis by clomiphene resensitizes resistant *S. pneumoniae* to amoxicillin**
599 We successfully exploited the knowledge gained on the mevalonate depletion phenotype to fight
600 amoxicillin-resistant *S. pneumoniae* strains. To do so, we confirmed that clomiphene, a compound known
601 to block Und-P production in *S. aureus*[33], elicits the elongated mevalonate depletion phenotype in *S.*

602 *pneumoniae* and therefore most likely also inhibits Und-P production in this bacterium. We next combined
603 clomiphene with the β-lactam antibiotic amoxicillin that preferentially interferes with cell division[64,65].
604 Results demonstrated that clomiphene can enhance the antimicrobial effect of amoxicillin in a D39V lab
605 strain, although this effect was rather limited. However, potentiation by clomiphene becomes much
606 stronger in amoxicillin-resistant strains such as 19F, Spain-23F and 11A. In *S. pneumoniae*, resistance
607 towards β-lactam antibiotics is mostly caused by mosaic penicillin binding proteins (PBPs). These
608 resistance-conferring mosaic PBPs are formed by recombination events following horizontal gene transfer
609 from β-lactam resistant donor strains[4,7]. We speculate that these mosaic PBPs display suboptimal activity
610 which allows them to remain active during amoxicillin treatment but fail to carry out their task if the
611 amount of peptidoglycan precursors available to them becomes limiting due to a deficiency in Und-P
612 production.
613
614 Whereas this combination treatment strategy works remarkably well *in vitro*, *in vivo* results using a murine
615 pneumonia disease model did not show benefits of combining amoxicillin treatment with clomiphene,
616 likely because the *in vivo* concentration of active clomiphene is too low. Nonetheless, we believe that
617 clomiphene represents a promising starting point for the development of an optimized antibacterial
618 compound that can be used in combination with amoxicillin and potentially other β-lactams. Clomiphene
619 is an FDA-approved prodrug that is administered as a racemic mixture of two stereoisomers and is
620 metabolized by the liver into active compounds that stimulate ovulation in anovulatory women[72-74,76].
621 However, since we observe antibacterial effects and amoxicillin potentiation *in vitro*, it seems likely that
622 one or both of the prodrug isomers exert the desired effect. Determining which clomiphene stereoisomer
623 has the highest antibacterial activity and designing non-metabolizable derivatives that are active at lower
624 concentrations would be the first step to further optimize the here proposed combination treatment
625 strategy for *in vivo* use. We hope that such an optimized antibacterial compound can be exploited for the
626 eradication of amoxicillin-resistant *S. pneumoniae* infections and could potentially also target other
627 species and/or strains with a different resistance profile towards β-lactam antibiotics. We therefore
628 believe that further investigation into this combination treatment strategy holds much promise in
629 combatting the ever-increasing amount of antibiotic-resistant bacterial infections.
630

631 **Materials & Methods**

632

633 **Bacterial strains and growth conditions**

634 All pneumococcal strains used in this work are listed in Table 2. Unless specified otherwise, strains used
635 throughout this work are derivatives of *S. pneumoniae* D39V[46]. In general, genomic changes were
636 introduced by homologous recombination after transformation of a linear DNA molecule into *S.*
637 *pneumoniae*. This linear DNA was either obtained through a one-step PCR reaction starting from a
638 different strain that already carried the desired transformation product (e.g. *hlpA-gfp* and *ftsZ-mCherry*)
639 or through golden gate cloning in which three different PCR products were ligated. The first and last of
640 these PCR products were homologous to the up- and downstream regions of the genome where a deletion
641 or insertion had to be made. In case of insertion of expression cassettes into the *zip* locus, these fragments
642 also contained a P_{lac} promoter and a spectinomycin (or trimethoprim) resistance marker through
643 amplification of fragments of the pPEPZ plasmid[50]. In case of insertion of expression cassettes into the
644 *bgaA* locus, these fragments also contained a P_{tet} promoter and a tetracycline resistance marker through
645 amplification of fragments from strain VL2212[23]. The third, middle fragment contained an antibiotic
646 marker or a sequence to be inserted into the genome. Golden gate cloning sites were introduced into the
647 PCR fragments as part of the primers. PCR fragments were digested with either BsaI, Esp3I or SapI,
648 followed by ligation and transformation. In case individual sgRNAs were cloned into *S. pneumoniae*, the
649 sgRNA sequences were first inserted into the pPEPZ-sgRNAclone plasmid in *E. coli*, as described
650 previously[23]. These integrative plasmids were then transformed into *S. pneumoniae*. Transformation was
651 performed with cells that were made competent by addition of the Competence Stimulating Peptide (CSP-
652 1) using a previously published protocol[77]. Primers that were used for cloning are listed in Table 3. *hlpA-*
653 *gfp* was amplified from VL2226 with primers OVL47&48. *ftsZ-mCherry* was amplified from VL1630 with
654 primers OVL898&901. Both PCR products were transformed to VL1998 to create VL3117.
655 Complementation constructs for mevalonate operon 1 (*mvaS-mvaA*) and operon 2 (*mvk-mvaD-mvaK2-*
656 *fni*) were made by amplification of the corresponding operons using primer pairs OVL3962&63 and
657 OVL3958&59, respectively. Up- and downstream regions for insertion into the *zip* locus were amplified
658 using primer pairs OVL3493&2181 and OVL2182&3496. For the complementation constructs of the *uppS*
659 and *mraY* genes that were amplified using primers OVL4583&84 and OVL4595&96, respectively, up- and
660 downstream regions of the *zip* locus were created using OVL3493&4341 and 2182&3496. The
661 complementation construct for SPV_1620 was created by amplification of the gene using OVL3671&72
662 and up- and downstream *zip* regions were produced using OVL3493&3650 and 3649&3496. Deletion of

663 the corresponding native genes was performed by replacing them with a promoter-less kanamycin
664 resistance cassette that was expressed using the native promoter of the deleted genes. The kanamycin
665 cassette was amplified from the pPEPY plasmid[50] with primers OVL3981&82. The up- and downstream
666 regions of the genes to be deleted were amplified using OVL4069&70 and OVL4071&72 for mevalonate
667 operon 1 (*mvaS-mvaA*), OVL4585&86 and OVL4587&88 for *uppS*, OVL4597&98 and OVL4599&4600 for
668 *mraY* and OVL3677&4601 and OVL 4602&3680 for *SPV_1620*. Due to low expression levels [78], mevalonate
669 operon 2 (*mvk-mvaD-mvaK2-fni*) was replaced with a Km cassette that carried its own constitutive
670 promoter. This fragment was amplified with OVL3983&82 from pPEPY[50] and up- and downstream regions
671 for this operon were amplified with primer pairs OVL4061&62 and OVL4063&64. A complementation
672 construct for *divIVA* was made by amplification of this gene using primers OVL5707 &08. Up- and
673 downstream regions for insertion into the *bgaA* locus were amplified using primer pairs
674 OVL2077&OVL5705 and OVL5706&1369. Deletion of *divIVA* was performed by replacement with a
675 promoter-less chloramphenicol resistance cassette that was expressed using the *divIVA* promoter. The
676 chloramphenicol cassette was amplified from VL3117 with primers OVL5727&28. The up- and
677 downstream regions of *divIVA* were amplified using OV5729&30 and OVL5731&32, respectively. A
678 complementation construct for *pbp2x* was made by amplification of this gene using primers OVL6276&77.
679 Up- and downstream regions for insertion into the *bgaA* locus were amplified using primer pairs
680 OVL2077&OVL5717 and OVL5718&1369. Deletion of *pbp2x* was performed by replacement with a
681 promoter-less erythromycin resistance cassette that was expressed using the *pbp2x* promoter. The
682 cassette was amplified from pJWV502[23] with primers OVL2933&34. The up- and downstream regions of
683 *pbp2x* were amplified using OV6214&15 and OVL6216&17, respectively.
684
685 Strains were grown in liquid C+Y medium (pH = 6.8)[79] at 37°C without shaking. Plating was performed
686 inside Columbia agar with 3% sheep blood and plates were incubated at 37°C in a controlled atmosphere
687 containing 5% CO_2.
688
689 Antibiotics for selection were used at the following concentrations: chloramphenicol (Cm) 3 µg/ml,
690 erythromycin (Ery) 0.5 µg/ml, gentamicin (Gm) 40µg/ml, kanamycin (Km) 150 µg/ml, spectinomycin (Spec)
691 100 µg/ml, tetracycline (Tc) 0.5 µg/ml, Trimethoprim (Trm) 10 µg/ml. When necessary, P_{lac} promoters
692 were induced with various amounts of IPTG; 1 mM IPTG for induction of dCas9 for the sCRilecs-seq
693 screens, 20 µM IPTG for complementation of mevalonate operon 1 (*mvaS*, *mvaZ*), 100 µM for
694 complementation of *uppS* and 1 mM IPTG for complementation of mevalonate operon 2 (*mvk*, *mvaD*,

695 *mvaK2*, *fni*), *mraY* or *SPV_1620*. When necessary, P_{tet} promoters were induced with 500 ng/ml
696 anhydrotetracycline (aTc). Where appropriate, mevalonic acid was added to cultures at the concentration
697 indicated in the text (ranging from 100 µM to 1 mM). When strains lacking the first mevalonate operon
698 had to be grown under non-limiting conditions, 1 mM mevalonic acid was used. The concentrations of
699 antibiotics and other compounds that were used to assess their antibacterial activity are indicated in the
700 main text and/or figures and/or figure legends.
701
702 **Table 2: *S. pneumoniae* strains used in this study.**

Strain	Genome	Reference
D39V	Serotype 2, wildtype	[46]
19F	Serotype 19F, clinical isolate	This work
Spain-23F	Serotype 23F, PMEN1, clinical isolate	German National Reference Center for Streptococci
11A	Serotype 11A, PMEN3, clinical isolate	German National Reference Center for Streptococci
VL333	D39V *prs1*::*lacI-tetR-Gm*	Lab collection
VL567	D39V Δ*cps*::*Cm*	[80]
VL1313	11A	[5]
VL1630	D39V *ftsZ-mCherry-Ery bgaA*::P_{zn}-*gfp-stkP*	Lab collection
VL1998	D39V *prs1*::F6-*lacI-Gm bgaA*::P_{lac}-*dCas9-Tc*	[21]
VL2226	D39V *hlpA-gfp-Cm*	[37]
VL3117	VL1998 *hlpA-gfp-Cm ftsZ-mCherry-Ery*	This work
VL3404	VL333 *hlpA-gfp-Cm ftsZ-mCherry-Ery*	This work
VL3565	VL3404 *zip*::P_{lac}-*mvk-mvaD-mvaK2-fni-Spec* Δ*mvk-mvaD-mvaK2-fni*::*Km*	This work
VL3567	VL3404 *zip*::P_{lac}-*mvaS-mvaA-Spec* Δ*mvaS-mvaA*::*Km*	This work
VL3584	VL3404 *zip*::P_{lac}-*uppS-Spec* Δ*uppS*::*Km*	This work
VL3585	VL3404 *zip*::P_{lac}-*mraY-Spec* Δ*mraY*::*Km*	This work
VL3586	VL3404 *zip*::P_{lac}-*SPV_1620-Trm* Δ*SPV_1620*::*Km*	This work
VL3671	VL3117 *zip*::P3-*sgRNA035*	This work
VL3672	VL3117 *zip*::P3-*sgRNA036*	This work
VL3673	VL3117 *zip*::P3-*sgRNA046*	This work
VL3674	VL3117 *zip*::P3-*sgRNA087*	This work
VL3675	VL3117 *zip*::P3-*sgRNA100*	This work
VL3676	VL3117 *zip*::P3-*sgRNA121*	This work
VL3677	VL3117 *zip*::P3-*sgRNA135*	This work
VL3678	VL3117 *zip*::P3-*sgRNA355*	This work
VL3679	VL3117 *zip*::P3-*sgRNA432*	This work
VL3680	VL3117 *zip*::P3-*sgRNA455*	This work
VL3681	VL3117 *zip*::P3-*sgRNA460*	This work
VL3682	VL3117 *zip*::P3-*sgRNA461*	This work
VL3683	VL3117 *zip*::P3-*sgRNA503*	This work
VL3684	VL3117 *zip*::P3-*sgRNA573*	This work

VL3685	VL3117 *zip*::P3-*sgRNA583*	This work
VL3686	VL3117 *zip*::P3-*sgRNA590*	This work
VL3687	VL3117 *zip*::P3-*sgRNA628*	This work
VL3688	VL3117 *zip*::P3-*sgRNA673*	This work
VL3689	VL3117 *zip*::P3-*sgRNA757*	This work
VL3690	VL3117 *zip*::P3-*sgRNA780*	This work
VL3691	VL3117 *zip*::P3-*sgRNA785*	This work
VL3692	VL3117 *zip*::P3-*sgRNA796*	This work
VL3693	VL3117 *zip*::P3-*sgRNA813*	This work
VL3694	VL3117 *zip*::P3-*sgRNA822*	This work
VL3695	VL3117 *zip*::P3-*sgRNA824*	This work
VL3696	VL3117 *zip*::P3-*sgRNA900*	This work
VL3697	VL3117 *zip*::P3-*sgRNA1019*	This work
VL3699	VL3117 *zip*::P3-*sgRNA1064*	This work
VL3700	VL3117 *zip*::P3-*sgRNA1236*	This work
VL3701	VL3117 *zip*::P3-*sgRNA1240*	This work
VL3702	VL333 Δ*mvaS-mvaA*::*Km*	This work
VL3708	VL333 *zip*::P_{lac}-*mvk-mvaD-mvaK2-fni-Spec* Δ*mvk-mvaD-mvaK2-fni*::*Km*	This work
VL3709	VL333 *zip*::P_{lac}-*mvaS-mvaA-Spec* Δ*mvaS-mvaA*::*Km*	This work
VL3710	VL333 *zip*::P_{lac}-*uppS-Spec* Δ*uppS*::*Km*	This work
VL3711	VL333 *zip*::P_{lac}-*mraY-Spec* Δ*mraY*::*Km*	This work
VL3712	VL333 *zip*::P_{lac}-*SPV_1620-Trm* Δ*SPV_1620*::*Km*	This work
VL3834	VL1998 Δ*mvaS-mvaA*::*Km*	This work
VL4273	VL333 *bgaA*::P_{tet}-*pbp2x-Tc* Δ*pbp2x::Ery*	This work
VL4274	VL3709 *bgaA*::P_{tet}-*pbp2x-Tc* Δ*pbp2x::Ery*	This work
LD0001	VL3709 *bgaA*::P_{tet}-*divIVA-Tc* Δ*divIVA::Cm*	This work

Table 3: Primers used in this study.

Primer	Sequence
OVL47	GATTGTAACCGATTCATCTG
OVL48	GGAATGCTTGGTCAAATCTA
OVL898	CCAACAAGCTTCACAAAATAAACCG
OVL901	CTTATCCGTTGCACGCTGACTC
OVL1369	GTCTTCTTTTTTACCTTTAGTAACTACTAATCCTGCAC
OVL2077	ATTCCTTCTTAACGCCCCAAGTTC
OVL2181	GCGTCACGTCTCAGCATTATTTTTCCTCCTTATTTAT
OVL2182	GCGTCACGTCTCACGGATCCCTCCAGTAACTCGAGAA
OVL2933	GATCGGTCTCGAGGAATTTTCATATGAACAAAAATATAAAATATTCTCAA
OVL2934	GATCGGTCTCGTTATTTCCTCCCGTTAAATAATAGATAACTATTAAAAAT
OVL3493	GCCAATAAATTGCTTCCTTGTTTT
OVL3496	ATGACACGGATTTTAAGAATAATTCTTTC
OVL3649	TGTGTGGCTCTTCGAGAACTCGAGAAAAAAAAACCGCGCCC
OVL3650	TGTGTGGCTCTTCGGTTTCATTATTTTTCCTCCTTATTTATTTAGATCTTAATTGTGAGC
OVL3671	CTGGTAGCTCTTCCAACATGCTGAAATGGGAAGACTTGCCTG

OVL3672	CTGGTAGCTCTTCCTCTTTATTTTAGTACCTCAAACACGGTT
OVL3677	GTATAGTAAGCTGGCAGAGAATATC
OVL3680	ATACTTTTTAGGGACAGGATCAC
OVL3958	GCGTCACGTCTCAATGCTCGTCTAGTAAAAGGAAAAAATGACAAAAAAA
OVL3959	GCGTCACGTCTCATCCGTTACGCCTTTTTCATCTGATCATTTG
OVL3962	GCGTCACGTCTCAATGCAGTATAGAACGATTTTTTACATGAATGATAAAACAG
OVL3963	GCGTCACGTCTCATCCGTTATGATCTTAAATTTTCGAGATAGCGCT
OVL3981	GCGTCACGTCTCAATGGCTAAAATGAGAATATCACCGG
OVL3982	GCGTCACGTCTCACTAAAACAATTCATCCAGTAAAATATAATATTTTATTTTCTCC
OVL3983	GCGTCACGTCTCAGAGGACGCGCAAGCTG
OVL4061	CACTACCAATTGGTGAAGTTGCT
OVL4062	GCGTCACGTCTCACCTCTTTTTCCTTTTACTAGACGAAAAAACGTC
OVL4063	GCGTCACGTCTCATTAGGGCGTAACCAGCGCC
OVL4064	TACAGGTACGATGATTTTGGTCGT
OVL4069	AGCTGAAGATAAAGCCTGTAACCA
OVL4070	GCGTCACGTCTCACCATGTAAAAAATCGTTCTATACTATTTTATCACAAATGG
OVL4071	GCGTCACGTCTCATTAGCATAAAAACTCAGACGAATCGGTCT
OVL4072	ACAGCGCCGATTATTTCCTTTG
OVL4341	GCGTCACGTCTCAATTTATTTAGATCTTAATTGTGAGCGCTC
OVL4583	GCGTCACGTCTCAAAATTTTTGAATAGGAATAAGATCATGTTTGGATTTT
OVL4584	GCGTCACGTCTCATCCGCTAAACTCCTCCAAATCGGCG
OVL4585	TCCAGATTTTTCTTATGAGGAAACCTTATT
OVL4586	GCGTCACGTCTCACCATGATCTTATTCCTATTCAAAAATCTATCGTTTCATT
OVL4587	GCGTCACGTCTCATTAGGGAGGAGTTTAGGAGGAAATATGACC
OVL4588	CTGTACTGTCAACTATCATAAAGATAATGGT
OVL4595	GCGTCACGTCTCAAAATATTAACTTTAGGAGACTAATATGTTTATTTCCATCAG
OVL4596	GCGTCACGTCTCATCCGTTACATCAAATACAAAATTGCGAGGGT
OVL4597	AGATTGCTGACGAGAAAAATGGTG
OVL4598	GCGTCACGTCTCACCATATTAGTCTCCTAAAGTTAATGTAATTTTTTTAATGTCC
OVL4599	GCGTCACGTCTCATTAGGAATGGCACCCTGATGTTTCA
OVL4600	AATAAATCATCCATGTTGTTAAAATTATTAAAATTGTTGT
OVL4601	GCGTCACGTCTCACCATGCTGTTCTCCTTTGTTTTTATTATAC
OVL4602	GCGTCACGTCTCATTAGAGTAGTCATAAGAAAATGAGTACAG
OVL5705	GCGTCAGGTCTCAATTTATTTAGATCTACTCTATCAATGATAGAGTTATTATACTCT
OVL5706	GCGTCAGGTCTCAGCGTAAGGAAATCCATTATGTACTATTTCTG
OVL5707	GCGTCAGGTCTCAAAATTTAAGTAAGTGAGGAATAGAATGCCAATTACA
OVL5708	GCGTCAGGTCTCAACGCCTACTTCTGGTTCTTCATACATTGGG
OVL5717	GCGTCACGTCTCAATTTATTTAGATCTACTCTATCAATGATAGAGTTATTATACTCT
OVL5718	GCGTCACGTCTCAGCGTAAGGAAATCCATTATGTACTATTTCTG
OVL5727	GCGTCAGGTCTCAATGAACTTTAATAAAATTGATTTAGACAATTGGAAGAG
OVL5728	GCGTCAGGTCTCATTATAAAAGCCAGTCATTAGGCCTATCT
OVL5729	CTCCTTTTTTAACTCCTTTTATCAATCCTCA
OVL5730	GCGTCAGGTCTCATCATTCTATTCCTCACTTACTTAATAATAACTGGACG
OVL5731	GCGTCAGGTCTCAATAACTCCAGTGCATCCGACAGG
OVL5732	ACCAAGTCCATTTCTTTACGTTTGAC
OVL6214	GCGCGTAAGATTGAGCAA

OVL6215	GATCGGTCTCATCCTATCTTACTCCGCTATTCTAATATTTTCA
OVL6216	GATCGGTCTCGATAAATCAAGGACATTAAAAAAATTACATTAACTT
OVL6217	ACATCACCCATAAAGACCTTG
OVL6276	GCGTCACGTCTCAAAATTTAGAATAGCGGAGTAAGATATGAAGTGG
OVL6277	GCGTCACGTCTCAACGCTTAGTCTCCTAAAGTTAATGTAATTTTTTTAATGTCC

705

706 **Mechanical disruption of *S. pneumoniae* cell chains**

707 Cultures were diluted 3x in PBS to a final volume of 1 ml in screw cap tubes. Tubes were placed into a
708 FastPrep-24™ 5G Instrument (MP Biomedicals) with QuickPrep-3 adapter and shaken with a speed of 6.0
709 m/s for 30 s. This protocol was validated using VL3117 that was grown for 3.5h in C+Y medium. Samples
710 were either subjected to mechanical chain disruption using the FastPrep-24™ 5G or not, after which both
711 samples were analyzed by microscopy and flow cytometry.

712

713 **Construction of the CRISPRi libraries**

714 CRISPRi libraries were constructed by transformation of the desired strains with a pool of 1499 different
715 pPEPZ integrative plasmids carrying constitutively-expressed sgRNA sequences that together target the
716 entire genome[23]. For the initial screen, D39V P_{lac}-*dcas9 hlpA-gfp ftsZ-mCherry* (VL3117) was transformed.
717 Our second sCRilecs-seq screen was performed after transformation of D39V P_{lac}-*dcas9* Δ*mvaS* Δ*mvaA*
718 (VL3834) in the presence of 1 mM mevalonic acid. For both libraries, at least 10^5 individual transformants
719 were obtained and collected.

720

721 **sCRilecs-seq screen**

722 The transformed D39V P_{lac}-*dcas9 hlpA-gfp ftsZ-mCherry* (VL3117) library was grown for 3.5h in C+Y
723 medium supplemented with 1 mM IPTG. The D39V P_{lac}-*dcas9* Δ*mvaS* Δ*mvaA* (VL3834) library was grown
724 for 3.5h in C+Y medium supplemented with 1 mM IPTG and 100 µM mevalonic acid. Cell chains were
725 mechanically disrupted (see "Mechanical disruption of *S. pneumoniae* cell chains") and further diluted
726 into PBS 3-10x based on culture density.

727 Cells were sorted using a FACSAria™ IIIu Cell Sorter (BD Biosciences) equipped with violet, blue and red
728 lasers and a 70 µm nozzle. In case of the D39V P_{lac}-*dcas9 hlpA-gfp ftsZ-mCherry* (VL3117) library, cells were
729 gated based on FSC, SSC and GFP fluorescence. For the D39V P_{lac}-*dcas9* Δ*mvaS* Δ*mvaA* (VL3834) library,
730 cells were gated based on FSC and SSC only. For both libraries, cells with the 10% highest and lowest FSC
731 values were collected, as well as 70% of the population located around the median FSC value. For the
732 D39V P_{lac}-*dcas9 hlpA-gfp ftsZ-mCherry* (VL3117) library, the same fractions for GFP and mCherry values
733 were also sorted. Flow rates and dilutions were adjusted to keep the efficiency of sorting as high as
734 possible (and certainly above 85%) while not exceeding a sorting time of 60 min per sample. For every
735 fraction, 1.5 x 10^6 cells were collected and 6 different biological repeats were performed.

736 Cells were collected into 2 ml tubes, centrifuged at 18000 g for 5 min and pellets were stored at -20°C.
737 Cells were lysed by dissolving pellets in 10 µl H_2O + 0.025% DOC + 0.05% SDS and incubating 20 min at
738 37°C, followed by 5 min incubation at 80°C. After samples were allowed to cool off, a colony PCR was
739 performed using primers that contain index and adapter sequences necessary for Illumina sequencing. 10
740 µl of the lysed cell mixture was added to the PCR reaction as input DNA and 30 PCR cycles were performed.
741 The amplicons were purified from a 2% agarose gel and Illumina sequenced on a MiniSeq according to
742 manufacturer's instructions. Sequencing was performed with a custom sequencing protocol[23].

743 Data analysis was performed as described previously[23]. The sgRNA sequences were recovered from the
744 resulting reads using Trimmomatic[81] and mapped onto the *S. pneumoniae* D39V genome using Bowtie2[82].
745 The mapped sgRNAs were counted using featureCounts[83] and the DESeq2 R package was used to define
746 enrichments and associated p values for every sgRNA[84]. For the initial sCRilecs-seq screen, we defined
747 significant hits as sgRNAs from the fraction with the highest or lowest FSC/GFP/mCherry values with an
748 adjusted p value < 0.1 and $Log_2FC > 1$ compared to counts from the corresponding control population. For
749 the second sCRilecs-seq screen performed with a Δ*mvaS-mvaA* mutant limits were set at an adjusted p
750 value < 0.05 and $Log_2FC > 1$.

751

752 **Flow cytometry**

753 Flow cytometry experiments were performed using NovoCyte 2100YB (ACEA Biosciences) flow cytometer
754 equipped with violet, blue and red lasers. To validate sCRilecs-seq hits, strains were grown for 3.5h in C+Y
755 medium with or without 1 mM IPTG. Cultures were diluted in PBS and cell chains were disrupted as
756 described above. Next, cells were incubated for 30 min at room temperature to mimic the average waiting
757 time in the 60 min sorting step before cell parameters (FSC, GFP and mCherry) were measured. Cell gatings
758 were chosen based on FSC, SSC and GFP values, as was done during sorting.
759
760 **Gene ontology enrichment analyses**
761 Gene ontology enrichment analyses were performed using the online Gene Ontology Resource platform
762 that is coupled to the PANTHER classification system analysis tool[42-44]. Validated significant sgRNA hits
763 were translated into the spr identifiers that correspond to the targeted genes, which were used as the
764 input gene set that was compared to the *S. pneumoniae* reference list provided by the platform. A
765 PANTHER overrepresentation analysis was performed to identify biological processes that are
766 overrepresented as defined by a Fisher's exact test using FDR-corrected p values. The significance cut-off
767 was set at adjusted p value < 0.05.
768
769 **OD growth curves**
770 Cultures were grown until OD_{595nm} 0.1 in C+Y medium under non-limiting conditions
771 (deletion/complementation strains were grown with the appropriate amount of IPTG, aTc or mevalonic
772 acid, as listed in "Bacterial strains and growth conditions"). Cultures were diluted 100x into C+Y medium
773 supplemented or not with IPTG, aTc or mevalonic acid and with or without the addition of antibacterial
774 compounds, as indicated in the text. 300 µl of cell suspension was transferred into 96-well plates. When
775 growth in the presence of BAL fluid was tested, cultures were diluted 100x into C+Y medium
776 supplemented with ¼ BAL fluid. 200 µl of cell suspension was transferred into 96-well plates. In both cases,
777 addition of compounds such as amoxicillin or clomiphene occurred at this stage by diluting stock
778 concentrations into the wells of the 96-well plates (dilutions were chosen to always keep the DMSO
779 concentrations in the wells ≤ 1%). Growth was monitored by measuring $OD_{595\ nm}$ every 10 min using a
780 TECAN Infinite F200 Pro. OD_{595nm} values were normalized so that the lowest value measured during the
781 first hour of growth was 0.001, the initial OD_{595nm} value of the inoculum. In case the area under the curve
782 needed to be calculated, values were log-transformed before this parameter was determined using
783 GraphPad Prism 9.
784

785 **Minimal Inhibitory Concentration (MIC) measurements**

786 MIC values were determined by constructing growth curves in C+Y medium (see above). The MIC was
787 taken to be the concentration of the tested compound where the maximum OD_{595nm} value obtained was
788 less than 10% of the maximal OD_{595nm} value obtained in the absence of the compound.

789

790 **Phase contrast and fluorescence microscopy**

791 For the determination of cell morphology and FtsZ localization, cultures were grown until $OD_{595\ nm}$ 0.1 in
792 C+Y medium under non-limiting conditions (deletion/complementation strains were grown with the
793 appropriate amount of IPTG or mevalonic acid, as listed in "Bacterial strains and growth conditions").
794 Cultures were then diluted 100x into C+Y medium supplemented or not with IPTG or mevalonic acid and
795 grown until the $OD_{595\ nm}$ of the wild-type strain reached 0.2. At this point, cultures were diluted to $OD_{595\ nm}$
796 of 0.1 and incubated for 45 min at 30°C in order to slow down growth prior to imaging. 1 ml of cell
797 suspension was spun down (10000 g for 2 min) and pellets were dissolved in 40 µl PBS. Cells were kept on
798 ice prior to imaging.

799 To investigate peptidoglycan production using FDAAs, cultures were grown until $OD_{595\ nm}$ 0.1 in C+Y
800 medium under non-limiting conditions (deletion/complementation strains were grown with the
801 appropriate amount of IPTG, as listed in "Bacterial strains and growth conditions"). Cultures were then
802 diluted 100x into C+Y medium without IPTG and grown until the $OD_{595\ nm}$ of the wild-type strain reached
803 0.1. At this point, 250 µM sBADA was added and cultures were incubated for 15 min at 37°C. Cells were
804 washed 3 times with cold PBS (centrifuge at 10000 g for 1 min at 4°C) and pellets were dissolved in C+Y
805 medium containing 250 µM RADA. After incubating cells for 15 min at 37°C, the three wash steps were
806 repeated. Pellets were dissolved in PBS and kept on ice prior to imaging.

807 Cells were imaged by placing 0.4 µl of cell suspension on pads made of PBS containing 1% agarose. Imaging
808 was performed using a Leica DMi8 microscope with a sCMOS DFC9000 (Leica) camera and a SOLA light
809 engine (Lumencor). Phase contrast images were acquired using transmission light with 100 ms exposure
810 time. Leica DMi8 filter sets were used as follows: mCherry (Chroma 49017, Ex: 560/40 nm, BS: LP 590 nm,
811 Em: LP 590 nm) with exposure time 700 msec, sBADA (Ex: 470/40 nm Chroma ET470/40x, BS: LP 498 Leica
812 11536022, Em: 520/40 nm Chroma ET520/40m) with exposure time 200 msec, and RADA (Chroma 49017,
813 Ex: 560/40 nm, BS: LP 590 nm, Em: LP 590 nm) with exposure time 100 msec. Images were processed
814 using ImageJ and deconvolution was performed using Huygens software (Scientific Volume Imaging) with
815 standard settings using 15 iterations for FtsZ-mCherry and sBADA and 25 iterations for RADA.
816 Quantification of cell length and other properties was done using MicrobeJ[85] and BactMAP[86].

817 For the analysis and statistical comparison of cell size across different mutants and conditions (Figure 1C,
818 Figure S1; Figure 3D, F and H; Figure S3A-D; Figure 5J; Figure 6A; Figure S6D), the following approach was
819 used[87]. For every mutant and/or condition, cell size was recorded for at least 3 biologically independent
820 repeats. The one exception is the depletion of *mraY* at time point 4.5h where only 2 independent repeats
821 could be analyzed. At this late time point, the culture is most often taken over by suppressor mutants with
822 normal morphology. Despite many attempts, we failed to obtain a third repeat in which the *mraY*
823 depletion phenotype was still apparent. For every repeat, at least 100 cells were recorded unless
824 mentioned otherwise and their average cell length was determined. These average cell lengths were used
825 to calculate the mean and SEM values that are shown in the main figures. The average cell lengths of each
826 repeat were also used to determine any statistically significant differences using a Wilcox test with FDR
827 corrected p values.
828
829 **Transmission electron microscopy**
830 Cultures were grown until $OD_{595\ nm}$ 0.1 in C+Y medium under non-limiting conditions
831 (deletion/complementation strains were grown with the appropriate amount of IPTG, as listed in
832 "Bacterial strains and growth conditions"). Cultures were then diluted 100x into C+Y medium without IPTG
833 and grown until the $OD_{595\ nm}$ of the wild-type strain reached 0.2. At this point, cultures were diluted to
834 $OD_{595\ nm}$ of 0.1 and incubated for 45 min at 30°C in order to slow down growth prior to imaging. 4 ml of
835 cell suspension was spun down at 10000 g and pellets were fixed in glutaraldehyde solution 2.5% (EMS)
836 and in osmium tetroxide 1% (EMS) with 1.5% of potassium ferrocyanide (Sigma) in phosphate buffer (PB
837 0.1 M [pH 7.4]) for 1h at room temperature. Samples were washed twice with H_2O and pellets were
838 embedded in agarose 2% (Sigma) in water, dehydrated in acetone solution (Sigma) at graded
839 concentrations (30% - 40 min; 70% - 40 min; 100% - 2x1h). This was followed by infiltration in Epon resin
840 (EMS) at graded concentrations (Epon 33% in acetone - 2h; Epon 66% in acetone - 4h; Epon 100% - 2x8h)
841 and finally polymerized for 48h at 60°C. Ultrathin sections of 50 nm thick were cut using a Leica Ultracut
842 (Leica Mikrosysteme GmbH), picked up on a copper slot grid 2x1mm (EMS) coated with a polystyrene film
843 (Sigma). Sections were post-stained with uranyl acetate (Sigma) 4% in H_2O for 10 min, rinsed several times
844 with H_2O followed by Reynolds lead citrate in H_2O (Sigma) for 10 min and rinsed several times with H_2O.
845 Micrographs were taken with a transmission electron microscope FEI CM100 (FEI) at an acceleration
846 voltage of 80 kV with a TVIPS TemCamF416 digital camera (TVIPS GmbH).
847

848 ***In vivo* experiments using a murine pneumonia disease model**

849 Male C57BL/6JRj mice (8 weeks old) (Janvier Laboratories, Saint Berthevin, France) were maintained in
850 individually ventilated cages and were handled in a vertical laminar flow cabinet (class II A2, ESCO,
851 Hatboro, PA). All experiments complied with national, institutional and European regulations and ethical
852 guidelines, were approved by our Institutional Animal Care and Use guidelines (D59-350009, Institut
853 Pasteur de Lille; Protocol APAFIS#16966 201805311410769_v3) and were conducted by qualified,
854 accredited personnel.

855 Mice were anesthetized by intraperitoneal injection of 1.25 mg (50 mg/kg) ketamine plus 0.25 mg (10
856 mg/kg) xylazine in 200 µl of PBS. Mice were infected intranasally with 30 µl of PBS containing 50 plaque-
857 forming units (PFUs) of the pathogenic murine-adapted H3N2 influenza A virus strain Scotland/20/74[71].
858 Seven days later, mice were inoculated intranasally with 10^5 CFU of *S. pneumoniae* strain 19F in 30 µl of
859 PBS. Mice were treated intragastrically with 5 mg of clomiphene (Clomid, Sanofi-Aventis, France) in 200
860 µl of water and or 1 mg of amoxicillin (Clamoxyl for injection, GlaxoSmithKline) in 200 µl of water at 8 and
861 12 hours post-infection, respectively. Mice were sacrificed 24 hours post-infection by intraperitoneal
862 injection of 5.47 mg of sodium pentobarbital in 100 µl PBS (Euthasol, Virbac, France). Bronchoalveolar
863 lavage fluids (BAL) were sampled after intratracheal injection of 1 mL of PBS and centrifugation at 1400
864 rpm for 10 min. Lungs and spleen were sampled to determine the bacterial load. Tissues were
865 homogenized with an UltraTurrax homogenizer (IKA-Werke, Staufen, Germany) and serial dilutions were
866 plated on blood agar plates and incubated at 37°C. Viable counts were determined 24h later. Statistical
867 significance between groups was calculated by the Kruskall-Wallis test (One-Way ANOVA). Analyses were
868 performed with Prism software (version 9, GraphPad Software, La Jolla, CA).

869

870

871 **Acknowledgements**

872 We thank Mark van der Linden, German National Reference Center for Streptococci for providing us with
873 the *S. pneumoniae* clinical isolates of Spain-23F and 11A strains and Frédéric Wallet, Regional Reference
874 Center for pneumococci, Lille, for providing the *S. pneumoniae* strain 19F. We thank Emanuele Cattani for
875 technical assistance, construction of strains VL3710, VL3711 and VL3712, and microscopy data used in
876 Figure S3C-D. Work in the Veening lab is supported by the Swiss National Science Foundation (SNSF)
877 (project grants 310030_200792 and 310030_192517), SNSF JPIAMR grant (40AR40_185533), SNSF NCCR
878 'AntiResist' (51NF40_180541) and ERC consolidator grant 771534-PneumoCaTChER. LD is the recipient of
879 a Marie Skłodowska Curie Actions – Individual Fellowship (MSCA-IF, proposal number 837923). JCS, MB,

and CC received funding from Région Hauts de France STaRS, and the European Union's Horizon 2020 research and innovation programme under grant agreement No 847786.

References

1 Weiser, J. N., Ferreira, D. M. & Paton, J. C. *Streptococcus pneumoniae*: transmission, colonization and invasion. *Nat Rev Microbiol* **16**, 355-367, doi:10.1038/s41579-018-0001-8 (2018).

2 O'Brien, K. L. *et al.* Burden of disease caused by *Streptococcus pneumoniae* in children younger than 5 years: global estimates. *Lancet* **374**, 893-902, doi:10.1016/S0140-6736(09)61204-6 (2009).

3 Bogaert, D., De Groot, R. & Hermans, P. W. *Streptococcus pneumoniae* colonisation: the key to pneumococcal disease. *Lancet Infect Dis* **4**, 144-154, doi:10.1016/S1473-3099(04)00938-7 (2004).

4 Jensen, A., Valdorsson, O., Frimodt-Moller, N., Hollingshead, S. & Kilian, M. Commensal streptococci serve as a reservoir for beta-lactam resistance genes in *Streptococcus pneumoniae*. *Antimicrob Agents Chemother* **59**, 3529-3540, doi:10.1128/AAC.00429-15 (2015).

5 Camara, J. *et al.* Evolution of the beta-lactam-resistant *Streptococcus pneumoniae* PMEN3 clone over a 30 year period in Barcelona, Spain. *J Antimicrob Chemother* **73**, 2941-2951, doi:10.1093/jac/dky305 (2018).

6 Schrag, S. J. *et al.* Emergence of *Streptococcus pneumoniae* with very-high-level resistance to penicillin. *Antimicrob Agents Chemother* **48**, 3016-3023, doi:10.1128/AAC.48.8.3016-3023.2004 (2004).

7 Hakenbeck, R., Bruckner, R., Denapaite, D. & Maurer, P. Molecular mechanisms of beta-lactam resistance in *Streptococcus pneumoniae*. *Future Microbiol* **7**, 395-410, doi:10.2217/fmb.12.2 (2012).

8 Kaur, R., Casey, J. R. & Pichichero, M. E. Emerging *Streptococcus pneumoniae* strains colonizing the nasopharynx in children after 13-valent pneumococcal conjugate vaccination in comparison to the 7-valent era, 2006-2015. *Pediatr Infect Dis J* **35**, 901-906, doi:10.1097/INF.0000000000001206 (2016).

9 Brueggemann, A. B., Pai, R., Crook, D. W. & Beall, B. Vaccine escape recombinants emerge after pneumococcal vaccination in the United States. *PLoS Pathog* **3**, e168, doi:10.1371/journal.ppat.0030168 (2007).

10 Hanage, W. P., Fraser, C., Tang, J., Connor, T. R. & Corander, J. Hyper-recombination, diversity, and antibiotic resistance in pneumococcus. *Science* **324**, 1454-1457, doi:10.1126/science.1171908 (2009).

11 Domenech, A. *et al.* Proton motive force disruptors block bacterial competence and horizontal gene transfer. *Cell Host Microbe* **27**, 544-555 e543, doi:10.1016/j.chom.2020.02.002 (2020).

12 Chi, F., Nolte, O., Bergmann, C., Ip, M. & Hakenbeck, R. Crossing the barrier: evolution and spread of a major class of mosaic *pbp2x* in *Streptococcus pneumoniae*, *S. mitis* and *S. oralis*. *Int J Med Microbiol* **297**, 503-512, doi:10.1016/j.ijmm.2007.02.009 (2007).

13 Prieto, J., Calvo, A. & Gomez-Lus, M. L. Antimicrobial resistance: a class effect? *J Antimicrob Chemother* **50 Suppl S2**, 7-12, doi:10.1093/jac/dkf508 (2002).

14 Baquero, F., Baquero-Artigao, G., Canton, R. & Garcia-Rey, C. Antibiotic consumption and resistance selection in *Streptococcus pneumoniae*. *J Antimicrob Chemother* **50 Suppl S2**, 27-37, doi:10.1093/jac/dkf504 (2002).

15 Jacobs, M. R. Building in efficacy: developing solutions to combat drug-resistant *S. pneumoniae*. *Clin Microbiol Infect* **10 Suppl 2**, 18-27, doi:10.1111/j.1470-9465.2004.00862.x (2004).

16 Bradley, J. S. *et al.* The management of community-acquired pneumonia in infants and children older than 3 months of age: clinical practice guidelines by the Pediatric Infectious Diseases Society and the Infectious Diseases Society of America. *Clin Infect Dis* **53**, e25-76, doi:10.1093/cid/cir531 (2011).
17 Thiem, U., Heppner, H. J. & Pientka, L. Elderly patients with community-acquired pneumonia: optimal treatment strategies. *Drugs Aging* **28**, 519-537, doi:10.2165/11591980-000000000-00000 (2011).
18 Qi, L. S. *et al.* Repurposing CRISPR as an RNA-guided platform for sequence-specific control of gene expression. *Cell* **152**, 1173-1183, doi:10.1016/j.cell.2013.02.022 (2013).
19 Peters, J. M. *et al.* A comprehensive, CRISPR-based functional analysis of essential genes in bacteria. *Cell* **165**, 1493-1506, doi:10.1016/j.cell.2016.05.003 (2016).
20 Bikard, D. *et al.* Programmable repression and activation of bacterial gene expression using an engineered CRISPR-Cas system. *Nucleic Acids Res* **41**, 7429-7437, doi:10.1093/nar/gkt520 (2013).
21 Liu, X. *et al.* High-throughput CRISPRi phenotyping identifies new essential genes in *Streptococcus pneumoniae*. *Mol Syst Biol* **13**, 931, doi:10.15252/msb.20167449 (2017).
22 Cui, L. *et al.* A CRISPRi screen in *E. coli* reveals sequence-specific toxicity of dCas9. *Nat Commun* **9**, 1912, doi:10.1038/s41467-018-04209-5 (2018).
23 Liu, X. *et al.* Exploration of bacterial bottlenecks and *Streptococcus pneumoniae* pathogenesis by CRISPRi-Seq. *Cell Host Microbe* **29**, 107-120 e106, doi:10.1016/j.chom.2020.10.001 (2021).
24 de Wet, T. J., Gobe, I., Mhlanga, M. M. & Warner, D. F. CRISPRi-Seq for the identification and characterisation of essential Mycobacterial genes and transcriptional units. *BioRxiv*, 358275, doi:https://doi.org/10.1101/358275 (2018).
25 Lee, H. H. *et al.* Functional genomics of the rapidly replicating bacterium *Vibrio natriegens* by CRISPRi. *Nat Microbiol* **4**, 1105-1113, doi:10.1038/s41564-019-0423-8 (2019).
26 Rousset, F. *et al.* Genome-wide CRISPR-dCas9 screens in *E. coli* identify essential genes and phage host factors. *PLoS Genet* **14**, e1007749, doi:10.1371/journal.pgen.1007749 (2018).
27 Wang, T. *et al.* Pooled CRISPR interference screening enables genome-scale functional genomics study in bacteria with superior performance. *Nat Commun* **9**, 2475, doi:10.1038/s41467-018-04899-x (2018).
28 Park, J. S. *et al.* A FACS-based genome-wide CRISPR screen reveals a requirement for COPI in *Chlamydia trachomatis* invasion. *iScience* **11**, 71-84, doi:10.1016/j.isci.2018.12.011 (2019).
29 Smith, L. M., Jackson, S. A., Gardner, P. P. & Fineran, P. C. SorTn-seq: a high-throughput functional genomics approach to discovering regulators of bacterial gene expression. *Nat Protoc*, doi:10.1038/s41596-021-00582-6 (2021).
30 Boronat, A. & Rodriguez-Concepcion, M. Terpenoid biosynthesis in prokaryotes. *Adv Biochem Eng Biotechnol* **148**, 3-18, doi:10.1007/10_2014_285 (2015).
31 Heuston, S., Begley, M., Gahan, C. G. M. & Hill, C. Isoprenoid biosynthesis in bacterial pathogens. *Microbiology (Reading)* **158**, 1389-1401, doi:10.1099/mic.0.051599-0 (2012).
32 Bouhss, A., Trunkfield, A. E., Bugg, T. D. & Mengin-Lecreulx, D. The biosynthesis of peptidoglycan lipid-linked intermediates. *FEMS Microbiol Rev* **32**, 208-233, doi:10.1111/j.1574-6976.2007.00089.x (2008).
33 Farha, M. A. *et al.* Antagonism screen for inhibitors of bacterial cell wall biogenesis uncovers an inhibitor of undecaprenyl diphosphate synthase. *Proc Natl Acad Sci U S A* **112**, 11048-11053, doi:10.1073/pnas.1511751112 (2015).
34 Sorg, R. A. & Veening, J. W. Microscale insights into pneumococcal antibiotic mutant selection windows. *Nat Commun* **6**, 8773, doi:10.1038/ncomms9773 (2015).

973 35 Brochado, A. R. *et al.* Species-specific activity of antibacterial drug combinations. *Nature* **559**,
974 259-263, doi:10.1038/s41586-018-0278-9 (2018).
975 36 Shi, H. *et al.* Deep phenotypic mapping of bacterial cytoskeletal mutants reveals physiological
976 robustness to cell size. *Curr Biol* **27**, 3419-3429 e3414, doi:10.1016/j.cub.2017.09.065 (2017).
977 37 Kjos, M. *et al.* Bright fluorescent *Streptococcus pneumoniae* for live-cell imaging of host-
978 pathogen interactions. *J Bacteriol* **197**, 807-818, doi:10.1128/JB.02221-14 (2015).
979 38 Beilharz, K., van Raaphorst, R., Kjos, M. & Veening, J. W. Red fluorescent proteins for gene
980 expression and protein localization studies in *Streptococcus pneumoniae* and efficient
981 transformation with DNA assembled via the Gibson Assembly method. *Appl Environ Microbiol*
982 **81**, 7244-7252, doi:10.1128/AEM.02033-15 (2015).
983 39 Massidda, O., Novakova, L. & Vollmer, W. From models to pathogens: how much have we
984 learned about *Streptococcus pneumoniae* cell division? *Environ Microbiol* **15**, 3133-3157,
985 doi:10.1111/1462-2920.12189 (2013).
986 40 Vollmer, W., Massidda, O. & Tomasz, A. The cell wall of *Streptococcus pneumoniae*. *Microbiol*
987 *Spectr* **7**, GPP3-0018-2018, doi:10.1128/microbiolspec.GPP3-0018-2018 (2019).
988 41 Brown, S., Santa Maria, J. P., Jr. & Walker, S. Wall teichoic acids of Gram-positive bacteria. *Annu*
989 *Rev Microbiol* **67**, 313-336, doi:10.1146/annurev-micro-092412-155620 (2013).
990 42 Ashburner, M. *et al.* Gene ontology: tool for the unification of biology. *Nat Genet* **25**, 25-29,
991 doi:10.1038/75556 (2000).
992 43 Mi, H., Muruganujan, A., Ebert, D., Huang, X. & Thomas, P. D. PANTHER version 14: more
993 genomes, a new PANTHER GO-slim and improvements in enrichment analysis tools. *Nucleic*
994 *Acids Res* **47**, 419-426, doi:10.1093/nar/gky1038 (2019).
995 44 Consortium, T. G. O. The Gene Ontology Resource: 20 years and still GOing strong. *Nucleic Acids*
996 *Res* **47**, 330-338, doi:10.1093/nar/gky1055 (2019).
997 45 Wilding, E. I. *et al.* Identification, evolution, and essentiality of the mevalonate pathway for
998 isopentenyl diphosphate biosynthesis in Gram-positive cocci. *J Bacteriol* **182**, 4319-4327,
999 doi:10.1128/jb.182.15.4319-4327.2000 (2000).
1000 46 Slager, J., Aprianto, R. & Veening, J. W. Deep genome annotation of the opportunistic human
1001 pathogen *Streptococcus pneumoniae* D39. *Nucleic Acids Res* **46**, 9971-9989,
1002 doi:10.1093/nar/gky725 (2018).
1003 47 Balibar, C. J., Shen, X. Y. & Tao, J. S. The mevalonate pathway of *Staphylococcus aureus*. *J*
1004 *Bacteriol* **191**, 851-861, doi:10.1128/Jb.01357-08 (2009).
1005 48 Yu, W. Q. *et al.* The mevalonate auxotrophic mutant of *Staphylococcus aureus* can adapt to
1006 mevalonate depletion. *Antimicrob Agents Ch* **57**, 5710-5713, doi:10.1128/Aac.00726-13 (2013).
1007 49 Reichert, S. *et al.* Genetic adaptation of a mevalonate pathway deficient mutant in
1008 *Staphylococcus aureus*. *Front Microbiol* **9**, 1539, doi:ARTN 1539
1009 10.3389/fmicb.2018.01539 (2018).
1010 50 Keller, L. E., Rueff, A. S., Kurushima, J. & Veening, J. W. Three new integration vectors and
1011 fluorescent proteins for use in the opportunistic human pathogen *Streptococcus pneumoniae*.
1012 *Genes (Basel)* **10**, 394, doi:10.3390/genes10050394 (2019).
1013 51 Kuru, E., Tekkam, S., Hall, E., Brun, Y. V. & Van Nieuwenhze, M. S. Synthesis of fluorescent D-
1014 amino acids and their use for probing peptidoglycan synthesis and bacterial growth *in situ*. *Nat*
1015 *Protoc* **10**, 33-52, doi:10.1038/nprot.2014.197 (2015).
1016 52 Wheeler, R., Mesnage, S., Boneca, I. G., Hobbs, J. K. & Foster, S. J. Super-resolution microscopy
1017 reveals cell wall dynamics and peptidoglycan architecture in ovococcal bacteria. *Mol Microbiol*
1018 **82**, 1096-1109, doi:10.1111/j.1365-2958.2011.07871.x (2011).
1019 53 Yao, Z., Kahne, D. & Kishony, R. Distinct single-cell morphological dynamics under beta-lactam
1020 antibiotics. *Mol Cell* **48**, 705-712, doi:10.1016/j.molcel.2012.09.016 (2012).

1021 54 Yother, J. Capsules of *Streptococcus pneumoniae* and other bacteria: paradigms for
1022 polysaccharide biosynthesis and regulation. *Annu Rev Microbiol* **65**, 563-581,
1023 doi:10.1146/annurev.micro.62.081307.162944 (2011).
1024 55 Denapaite, D., Bruckner, R., Hakenbeck, R. & Vollmer, W. Biosynthesis of teichoic acids in
1025 *Streptococcus pneumoniae* and closely related species: lessons from genomes. *Microb Drug*
1026 *Resist* **18**, 344-358, doi:10.1089/mdr.2012.0026 (2012).
1027 56 Beilharz, K. *et al.* Control of cell division in *Streptococcus pneumoniae* by the conserved Ser/Thr
1028 protein kinase StkP. *Proc Natl Acad Sci U S A* **109**, E905-913, doi:10.1073/pnas.1119172109
1029 (2012).
1030 57 Fleurie, A. *et al.* Mutational dissection of the S/T-kinase StkP reveals crucial roles in cell division
1031 of *Streptococcus pneumoniae*. *Mol Microbiol* **83**, 746-758, doi:10.1111/j.1365-
1032 2958.2011.07962.x (2012).
1033 58 Fleurie, A. *et al.* Interplay of the serine/threonine-kinase StkP and the paralogs DivIVA and GpsB
1034 in pneumococcal cell elongation and division. *PLoS Genet* **10**, e1004275,
1035 doi:10.1371/journal.pgen.1004275 (2014).
1036 59 Novakova, L. *et al.* Identification of multiple substrates of the StkP Ser/Thr protein kinase in
1037 *Streptococcus pneumoniae*. *J Bacteriol* **192**, 3629-3638, doi:10.1128/JB.01564-09 (2010).
1038 60 Cho, H. *et al.* Bacterial cell wall biogenesis is mediated by SEDS and PBP polymerase families
1039 functioning semi-autonomously. *Nat Microbiol* **1**, 16172, doi:10.1038/nmicrobiol.2016.172
1040 (2016).
1041 61 Meeske, A. J. *et al.* SEDS proteins are a widespread family of bacterial cell wall polymerases.
1042 *Nature* **537**, 634-638, doi:10.1038/nature19331 (2016).
1043 62 Taguchi, A. *et al.* FtsW is a peptidoglycan polymerase that is functional only in complex with its
1044 cognate penicillin-binding protein. *Nat Microbiol* **4**, 587-594, doi:10.1038/s41564-018-0345-x
1045 (2019).
1046 63 Tsui, H. C. *et al.* Suppression of a deletion mutation in the gene encoding essential PBP2b reveals
1047 a new lytic transglycosylase involved in peripheral peptidoglycan synthesis in *Streptococcus*
1048 *pneumoniae* D39. *Mol Microbiol* **100**, 1039-1065, doi:10.1111/mmi.13366 (2016).
1049 64 Berg, K. H., Stamsas, G. A., Straume, D. & Havarstein, L. S. Effects of low PBP2b levels on cell
1050 morphology and peptidoglycan composition in *Streptococcus pneumoniae* R6. *J Bacteriol* **195**,
1051 4342-4354, doi:10.1128/JB.00184-13 (2013).
1052 65 Kocaoglu, O., Tsui, H. C., Winkler, M. E. & Carlson, E. E. Profiling of beta-lactam selectivity for
1053 penicillin-binding proteins in *Streptococcus pneumoniae* D39. *Antimicrob Agents Chemother* **59**,
1054 3548-3555, doi:10.1128/AAC.05142-14 (2015).
1055 66 Masadeh, M., Mhaidat, N., Alzoubi, K., Al-Azzam, S. & Alnasser, Z. Antibacterial activity of
1056 statins: a comparative study of atorvastatin, simvastatin, and rosuvastatin. *Ann Clin Microbiol*
1057 *Antimicrob* **11**, 13, doi:10.1186/1476-0711-11-13 (2012).
1058 67 Bergman, P. *et al.* Studies on the antibacterial effects of statins - *in vitro* and *in vivo*. *PLoS One* **6**,
1059 e24394, doi:10.1371/journal.pone.0024394 (2011).
1060 68 Kaneko, M., Togashi, N., Hamashima, H., Hirohara, M. & Inoue, Y. Effect of farnesol on
1061 mevalonate pathway of *Staphylococcus aureus*. *J Antibiot (Tokyo)* **64**, 547-549,
1062 doi:10.1038/ja.2011.49 (2011).
1063 69 Imohl, M., Reinert, R. R. & van der Linden, M. Serotype-specific penicillin resistance of
1064 *Streptococcus pneumoniae* in Germany from 1992 to 2008. *Int J Med Microbiol* **300**, 324-330,
1065 doi:10.1016/j.ijmm.2009.11.004 (2010).
1066 70 EUCAST. Breakpoint tables for interpretation of MICs and zone diameters, version 11.0.
1067 http://www.eucast.org/clinical_breakpoints/ (2021).

1068 71 Matarazzo, L. *et al.* Therapeutic synergy between antibiotics and pulmonary Toll-like receptor 5
1069 stimulation in antibiotic-sensitive or -resistant pneumonia. *Front Immunol* **10**, 723,
1070 doi:10.3389/fimmu.2019.00723 (2019).
1071 72 Dickey, R. P. & Holtkamp, D. E. Development, pharmacology and clinical experience with
1072 clomiphene citrate. *Hum Reprod Update* **2**, 483-506, doi:10.1093/humupd/2.6.483 (1996).
1073 73 Huppert, L. C. Induction of ovulation with clomiphene citrate. *Fertil Steril* **31**, 1-8,
1074 doi:10.1016/s0015-0282(16)43749-0 (1979).
1075 74 Nasseri, S. & Ledger, W. L. Clomiphene citrate in the twenty-first century. *Hum Fertil (Camb)* **4**,
1076 145-151, doi:10.1080/1464727012000199212 (2001).
1077 75 Zucchini, L. *et al.* PASTA repeats of the protein kinase StkP interconnect cell constriction and
1078 separation of *Streptococcus pneumoniae*. *Nat Microbiol* **3**, 197-209, doi:10.1038/s41564-017-
1079 0069-3 (2018).
1080 76 Murdter, T. E. *et al.* Genetic polymorphism of cytochrome P450 2D6 determines oestrogen
1081 receptor activity of the major infertility drug clomiphene via its active metabolites. *Hum Mol*
1082 *Genet* **21**, 1145-1154, doi:10.1093/hmg/ddr543 (2012).
1083 77 Synefiaridou, D. & Veening, J.-W. Harnessing CRISPR-Cas9 for genome editing in *Streptococcus*
1084 *pneumoniae* D39V. *Appl Environ Microbiol* **87**, e02762-02720, doi:10.1101/2020.06.13.149682
1085 %J bioRxiv (2020).
1086 78 Aprianto, R., Slager, J., Holsappel, S. & Veening, J. W. High-resolution analysis of the
1087 pneumococcal transcriptome under a wide range of infection-relevant conditions. *Nucleic Acids*
1088 *Res* **46**, 9990-10006, doi:10.1093/nar/gky750 (2018).
1089 79 Domenech, A., Slager, J. & Veening, J. W. Antibiotic-induced cell chaining triggers pneumococcal
1090 competence by reshaping quorum sensing to autocrine-like signaling. *Cell Rep* **25**, 2390-2400
1091 e2393, doi:10.1016/j.celrep.2018.11.007 (2018).
1092 80 Moreno-Gamez, S. *et al.* Quorum sensing integrates environmental cues, cell density and cell
1093 history to control bacterial competence. *Nat Commun* **8**, 854, doi:10.1038/s41467-017-00903-y
1094 (2017).
1095 81 Bolger, A. M., Lohse, M. & Usadel, B. Trimmomatic: a flexible trimmer for Illumina sequence
1096 data. *Bioinformatics* **30**, 2114-2120, doi:10.1093/bioinformatics/btu170 (2014).
1097 82 Langmead, B. & Salzberg, S. L. Fast gapped-read alignment with Bowtie 2. *Nat Methods* **9**, 357-
1098 359, doi:10.1038/nmeth.1923 (2012).
1099 83 Liao, Y., Smyth, G. K. & Shi, W. featureCounts: an efficient general purpose program for
1100 assigning sequence reads to genomic features. *Bioinformatics* **30**, 923-930,
1101 doi:10.1093/bioinformatics/btt656 (2014).
1102 84 Love, M. I., Huber, W. & Anders, S. Moderated estimation of fold change and dispersion for
1103 RNA-seq data with DESeq2. *Genome Biol* **15**, 550, doi:10.1186/s13059-014-0550-8 (2014).
1104 85 Ducret, A., Quardokus, E. M. & Brun, Y. V. MicrobeJ, a tool for high throughput bacterial cell
1105 detection and quantitative analysis. *Nat Microbiol* **1**, 16077, doi:10.1038/nmicrobiol.2016.77
1106 (2016).
1107 86 van Raaphorst, R., Kjos, M. & Veening, J. W. BactMAP: An R package for integrating, analyzing
1108 and visualizing bacterial microscopy data. *Mol Microbiol* **113**, 297-308, doi:10.1111/mmi.14417
1109 (2020).
1110 87 Lord, S. J., Velle, K. B., Mullins, R. D. & Fritz-Laylin, L. K. SuperPlots: Communicating
1111 reproducibility and variability in cell biology. *J Cell Biol* **219**, e202001064,
1112 doi:10.1083/jcb.202001064 (2020).
1113